Received: 23 October 2020 | Revised: 19 March 2021 | Accepted: 16 April 2021

DOI: 10.1002/hyp.14183

RESEARCH ARTICLE

WILEY

Lateral terrestrial water flow contribution to summer precipitation at continental scale – A comparison between Europe and West Africa with WRF-Hydro-tag ensembles

Joël Arnault[1] | Benjamin Fersch[1] | Thomas Rummler[2] | Zhenyu Zhang[1,2] | Gandome Mayeul Quenum[3] | Jianhui Wei[1] | Maximilian Graf[1,2] | Patrick Laux[1,2] | Harald Kunstmann[1,2]

[1]Institute of Meteorology and Climate Research, Karlsruhe Institute of Technology, Garmisch-Partenkirchen, Germany

[2]Institute of Geography, University of Augsburg, Augsburg, Germany

[3]National Institute of Water, Laboratory of Applied Hydrology, University of Abomey-Calavi Faculty of Science and Technology, Cotonou, Benin

Correspondence
Joël Arnault, Institute of Meteorology and Climate Research, Karlsruhe Institute of Technology, Kreuzeckbahnstraße 19, Garmisch-Partenkirchen, Germany.
Email: joel.arnault@kit.edu

Funding information
German Science Foundation, Grant/Award Number: DFG, AR 1183/2-1)

Abstract

It is well accepted that summer precipitation can be altered by soil moisture condition. Coupled land surface – atmospheric models have been routinely used to quantify soil moisture – precipitation feedback processes. However, most of the land surface models (LSMs) assume a vertical soil water transport and neglect lateral terrestrial water flow at the surface and in the subsurface, which potentially reduces the realism of the simulated soil moisture – precipitation feedback. In this study, the contribution of lateral terrestrial water flow to summer precipitation is assessed in two different climatic regions, Europe and West Africa, for the period June–September 2008. A version of the coupled atmospheric-hydrological model WRF-Hydro with an option to tag and trace land surface evaporation in the modelled atmosphere, named WRF-Hydro-tag, is employed. An ensemble of 30 simulations with terrestrial routing and 30 simulations without terrestrial routing is generated with random realizations of turbulent energy with the stochastic kinetic energy backscatter scheme, for both Europe and West Africa. The ensemble size allows to extract random noise from continental-scale averaged modelled precipitation. It is found that lateral terrestrial water flow increases the relative contribution of land surface evaporation to precipitation by 3.6% in Europe and 5.6% in West Africa, which enhances a positive soil moisture – precipitation feedback and generates more uncertainty in modelled precipitation, as diagnosed by a slight increase in normalized ensemble spread. This study demonstrates the small but non-negligible contribution of lateral terrestrial water flow to precipitation at continental scale.

KEYWORDS
continental scale, coupled modelling, ensemble, feedback, summer precipitation, terrestrial hydrology

Special Issue: Coupled atmosphere-hydrological processes: Novel system developments and cross-compartment evaluations.

1 | INTRODUCTION

The interaction between soil moisture and climate has been a subject of debate in the scientific community for several decades (e.g., Seneviratne et al., 2010), as a better knowledge of the state of the land surface can potentially improve climate model skills (e.g., Berg et al., 2016; Dirmeyer et al., 2009; Zhou et al., 2019). This is especially relevant in the context of global warming and drying trend in soils, which creates more locations with soil moisture-limited evaporation regime and enhances the soil moisture – precipitation feedback (e.g., Berg et al., 2016; Dirmeyer et al., 2012, 2013; Zhou et al., 2019).

According to a recent analysis from Hsu et al. (2017), two concurrent soil moisture – precipitation feedback processes can affect the amount of precipitation in a region. On the one hand, an increase in soil wetness can favour an increase in precipitation through a positive feedback process. On the other hand, an increase in soil dryness and soil moisture heterogeneity can also favour an increase in precipitation through a negative feedback process involving a change in low-level moisture convergence, as was also pointed out by Taylor et al. (2012). Nevertheless, at global scale the positive feedback process is expected to dominate, and the global negative trend in soil moisture is expected to reduce the overall land precipitation (Berg et al., 2016; Zhou et al., 2019).

The control of soil moisture on precipitation can also act remotely, as precipitation can be much sensitive to nonlocal land surface evaporation in a radius of the order of 1000 km (Wei & Dirmeyer, 2019). Soil moisture variability even has the potential to modify the large-scale atmospheric circulation and further impact precipitation remotely (e.g., Berg et al., 2017; Koster et al., 2016; Teng et al., 2019).

Berg et al. (2016) and Zhou et al. (2019) recommended that future developments in climate modelling should focus on improving the representation of land processes in order to better constrain the simulated soil moisture – precipitation feedback and improve the accuracy of the simulated climate. Traditional climate models use a soil column in order to represent terrestrial hydrology, which assumes that soil moisture can be transported only vertically. Such an approximation oversimplifies the terrestrial water compartment and may distort the entire hydrologic cycle in the model, especially precipitation in case of strong land – atmosphere coupling.

Coupled atmospheric-hydrological models have been developed in order to relax the purely vertical terrestrial water flow hypothesis with the description of lateral terrestrial water flow (e.g., Anyah et al., 2008; Davison et al., 2018; Gochis et al., 2018; Larsen et al., 2016; Maxwell et al., 2011; Rahman et al., 2015; Wagner et al., 2016). In particular, the hydrologically-enhanced WRF-Hydro model allows to consider overland and subsurface flow within the modelled land – atmosphere system (Gochis et al., 2018).

Arnault et al. (2018), Arnault, Wagner, et al. (2016), Fersch et al. (2020), Larsen et al. (2016), Rummler et al. (2019), Sulis et al. (2018), Zhang et al. (2019), among others, found that the consideration of lateral terrestrial water flow generally increases the soil water storage and surface evaporation, which potentially affects precipitation through regional recycling (e.g., Trenberth, 1999). In the case of Central Europe, Arnault et al. (2018) showed that the largest impact of lateral terrestrial water flow on modelled precipitation uncertainty occurs when surface flux spatial heterogeneity is high and the weather regime is dominated by local processes.

The contribution of a region's surface evaporation to a region's precipitation, namely the regional precipitation recycling, can be assessed with a tagging procedure within a climate model (e.g., Arnault et al., 2019; Arnault, Knoche, et al., 2016; Dominguez et al., 2016; Insua-Costa & Miguez-Macho, 2018; Knoche & Kunstmann, 2013; Sodemann et al., 2009; Wei et al., 2015, 2016). This procedure consists in selecting a source of tagged evaporation and following the fate of the tagged water through the atmospheric water compartments of the climate model. Applying the version of WRF-Hydro enhanced with a tagging procedure (WRF-Hydro-tag, Arnault, Knoche, et al., 2016; Arnault et al., 2019) to the land surface evaporation occurring in a 10 000 km^2 drainage area in northern China, Zhang et al. (2019) found that lateral terrestrial water flow increases the regional precipitation recycling from 1.3% to 1.7% during the summer time.

Regional precipitation recycling increases with the region's size (e.g., Arnault, Knoche, et al., 2016; Trenberth, 1999). Therefore, a simulation domain covering a large land surface area, such as a continental-scale domain, would be necessary in order to fully represent the land surface evaporation change driven by lateral terrestrial water flow and assess the resulting impact on precipitation. In a continental-scale coupled atmospheric-hydrological simulation for North America, Anyah et al. (2008) found a larger control of groundwater table depths on surface evaporation and convective precipitation in the arid west.

The present paper aims at further evaluating the contribution of lateral terrestrial water flow to precipitation for two continental-scale regions: Europe and West Africa, using simulations' ensembles with WRF-Hydro-tag. The choice of a mid-latitude and a tropical region aims at highlighting a potential climate-dependency of the role of lateral terrestrial water flow in the hydrologic cycle. The study period is set to four summer months from June to September 2008, in order to assess the connection between lateral terrestrial water flow and precipitation at a time of the year when the coupling between the land surface and the atmosphere is most active (e.g., Gerken et al., 2019). The aim of generating simulations' ensembles is twofold, (1) to disentangle the respective effects of modelled atmospheric randomness (e.g., Rasmussen et al., 2012) and lateral terrestrial water flow on precipitation, and (2) to assess the effect of lateral terrestrial water flow on modelled precipitation uncertainty as in Arnault et al. (2018). The choice of WRF-Hydro-tag to generate the simulations' ensembles is motivated by two model options: (1) to activate or deactivate overland and subsurface flow routing during the model run, which facilitates the sensitivity analysis of model results to lateral terrestrial water flow; and (2) to tag and trace land surface evaporation, which allows to evaluate the differences in atmospheric water pathways between simulations including lateral terrestrial water flow or not.

Details on the numerical simulations and method of analysis are given in Section 2. Results are discussed in Section 3, and conclusive remarks are finally provided in Section 4.

2 | METHOD

2.1 | Model description

WRF-Hydro-tag is a version of the Weather Research and Forecasting model (WRF, Skamarock & Klemp, 2008) enhanced with the description of lateral terrestrial water flow (Gochis et al., 2018) and with a soil-vegetation-atmosphere water tagging procedure (Arnault et al., 2019). This tagging procedure consists in implementing prognostic equations of tagged water, defining a source of tagged water for a given area and a given period in order to initialize the tagged water cycle, and assessing the fate of the water source via the tagged water cycle during the model run. Two tagging options are currently considered in the tagging procedure of WRF-Hydro-tag, the surface evaporation tagging option which consists in tracing a region's surface evaporation in the atmosphere, and the precipitation tagging option which consists in tracing a region's precipitation in the soil and in the atmosphere for the evaporated part. In this study, WRF-Hydro-tag is used with the surface evaporation tagging option.

As WRF, WRF-Hydro-tag is a limited-area modelling system which requires three-dimensional meteorological driving data and allows to simulate the land – atmosphere system of a selected region for a selected time period. WRF-Hydro-tag can be run with or without spatial re-distribution of terrestrial water through overland or subsurface flow. In the following, the model configuration with disabled computation of lateral terrestrial water flow is referred to as WRF-tag, and the model configuration with enabled computation of lateral terrestrial water flow is referred to as WRF-Hydro-tag.

The original development of WRF-tag and WRF-Hydro-tag (Arnault et al., 2019) was based on WRF version 3.7, hydrological modules of WRF-Hydro version 3.0, and the following setup of WRF physics parameterisation options: six-class WSM6 microphysics scheme of Hong and Lim (2006), ACM2 planetary boundary layer scheme of Pleim (2007), and Noah land surface model (LSM) of Chen and Dudhia (2001). For this study the tagging procedure of WRF-Hydro-tag is adapted to the WSM6 scheme, ACM2 scheme, and the community Noah LSM with multi-parameterization options (Noah-MP, Niu et al., 2011) of WRF version 4.0, and the hydrological module of WRF-Hydro version 5.0.

2.2 | Study regions and observational datasets

Summer precipitation in Europe is governed by a weak westerly flow regime and local processes (e.g., Zveryaev & Allan, 2010), whereas summer precipitation in West Africa is governed by a steady easterly flow regime and a monsoonal circulation, and local processes as well (e.g., Xue et al., 2012). In order to simulate these two summer precipitation regimes with WRF-tag and WRF-Hydro-tag, the two domains depicted in Figure 1 are selected. These two domains are characterized by the same size and cover an area of 3500 km $\times$ 2500 km each.

For Europe, most of the land area in the selected domain is surrounded by sea and ocean water, especially at the western border where the large-scale atmospheric disturbances originate from. This suggests that the domain size is enough to assess the full effect of lateral terrestrial water flow on land surface evaporation and precipitation in Europe.

For West Africa, the eastern part of the African continent is not included in the selected domain. This means that, with this domain size, it would not be possible to evaluate the contribution of land surface evaporation changes induced by lateral terrestrial water flow in East Africa to precipitation in West Africa. Still, we emphasize that using the same domain size for both study regions facilitates the comparison of model results, with the final objective to better understand the specific physical processes through which lateral terrestrial water flow contributes to precipitation in these two different climatic regions.

The skill of WRF-tag and WRF-Hydro-tag in correctly representing coupled land – atmosphere processes occurring in the study regions is assessed by comparing the simulated land surface evaporation and precipitation with gridded datasets. For land surface evaporation, we use the product from the FLUXNET Model Tree Ensemble (MTE, Jung et al., 2009, 2010) which provides a global coverage of monthly sums of land surface evaporation at a spatial resolution of 0.5°. For precipitation in Europe, we use the product from the European Climate Assessment & Dataset project (Haylock et al., 2008) which provides daily precipitation sums at a spatial resolution of 0.25° over the European region. For precipitation in West Africa, we use the climate hazards infrared precipitation with stations (CHIRPS, Funk et al., 2015) dataset which provides daily precipitation sums at a spatial resolution of 0.05° within the latitudinal band between 50°S and 50°N. In the following, observational land surface evaporation is named E_{OBS} (m/s), and observational precipitation P_{OBS} (m/s).

2.3 | Model setup

For both Europe and West Africa, we use the same WRF-tag and WRF-Hydro-tag setups. Concerning the atmospheric part in WRF-tag and WRF-Hydro-tag, the equations of atmospheric motions are resolved on a three-dimensional grid characterized by 700 $\times$ 500 horizontal grid points with a 5 km grid spacing and 50 vertical levels from the near-surface up to 10 hPa, using a timestep of 30 s. The subgrid-scale atmospheric processes accounted for are the long and short wave radiative fluxes with the schemes of Mlawer et al. (1997) and Dudhia (1989), microphysics with the WSM6 scheme, and atmospheric turbulence with the ACM2 scheme. The lateral boundary condition of atmospheric variables is prescribed at a 6 hourly time

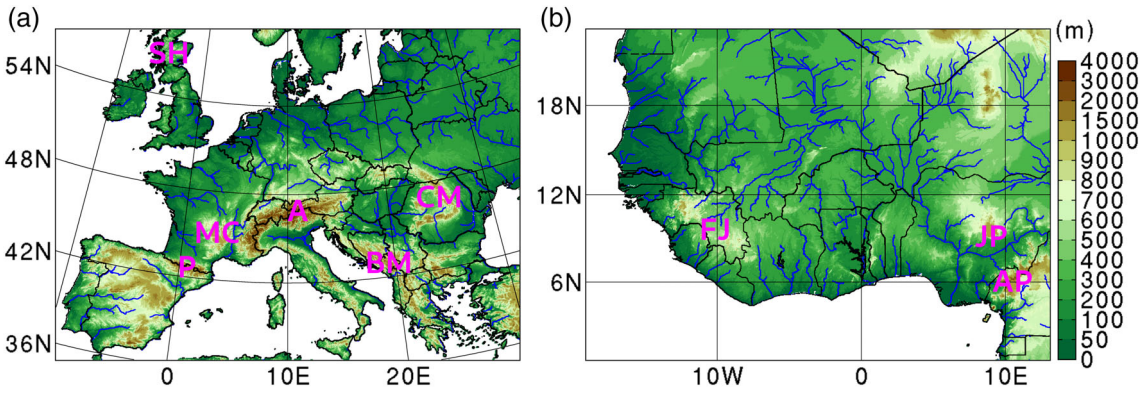

FIGURE 1 (a) Terrain elevation of the simulation's domain for Europe, given in meter above sea level. The solid black lines delineate the political boundaries, and the solid blue lines indicate the river channels with Strahler stream order equal to or above 7. (b) As in (a) except for West Africa. Magenta labels indicate locations of mountain ranges quoted in the text: A, Alps; AP, Adamawa Plateau; BM, Balkan Mountains; CM, Carpathian Mountains; FJ, Fouta Djallon; JP, Jos Plateau; MC, Massif Central; P, Pyrenees; SH, Scottish Highlands

interval with the ERA5 reanalyses (Copernicus Climate Change Service, 2017). The simulation period extends from 1 January to 1 October 2008, the first 5 months being considered as a spinup period for the simulated land – atmosphere exchange processes. The last 4 months from June to September is the study period. Arnault et al. (2018) and Arnault, Wagner, et al. (2016) brought evidence that a spinup period of a few months is sufficient to simulate realistic land surface conditions in Europe and West Africa with WRF-Hydro. In this study, the five-month spinup period is chosen as a compromise between the two-week spinup period employed for example in Camera et al. (2020), and a one-year spinup period employed for example in Rummler et al. (2019).

For the water tagging procedure, the tagged atmospheric water variables are initially set to zero and the land surface evaporation occurring over the simulation's domain during the model run is set as the source of tagged water vapour. The tagged water variables in model outputs allow to assess the fate of land surface evaporation in the simulated atmosphere, until it reaches the lateral boundary of the simulation's domain or reaches the surface as precipitation (e.g., Arnault, Knoche, et al., 2016; Zhang et al., 2019).

Concerning the land surface part commonly shared by WRF-tag and WRF-Hydro-tag, Noah-MP (Niu et al., 2011) is chosen in order to describe the fate of snow cover, vegetation canopy, and soil moisture within a soil column of 2 m-depth, and to provide the land surface boundary condition of atmospheric fluxes. Distributed model parameters, such as the roughness length, root depth or soil hydraulic conductivity, are prescribed as a function of landuse classes from the moderate resolution imaging spectroradiometer (MODIS) land cover map (Friedl et al., 2002), and soil classes from the State Soil Geographic / Food and Agriculture Organization soil database (FAO, 1991). The Noah-MP parameterisation options selected are the default ones, as described in Cuntz et al. (2016), except for the activation of a dynamic vegetation model (Niu et al., 2011) which provides estimates of vegetation cover and leaf area index independently of table values, the leaf area index being initialized with the satellite-derived climatology from Kumar et al. (2014). The other land surface variables of Noah-MP are initialized with the ERA5 reanalyses. The equations describing the fate of these land surface variables are resolved using a timestep of 30 s, as for the atmospheric processes, in order to reduce numerical uncertainty in the modelled land – atmosphere coupling.

Using the WRF-Hydro hydrological modules (Gochis et al., 2018), WRF-Hydro-tag, further considers the description of overland and subsurface flow on a subgrid. This subgrid is generated with the WRF-Hydro Pre-processing Tool and using the digital elevation data from the hydrological data and maps based on Shuttle Elevation Derivatives at Multiple Scales (HydroSHEDS) data base (Lehner et al., 2008), and is characterized by 14 000 $\times$ 10 000 horizontal grid points with a 250 m grid spacing and a minimal number of pixels to define a stream set to 16. The location of the main river channels obtained with this method are displayed in Figure 1. At each timestep, surface water and liquid soil moisture variables are disaggregated to the finer subgrid using linear weighting factors. Surface and subsurface routing is then performed by taking into account exfiltration from saturated soil columns and river channel inflow, resulting in updated fields for liquid soil moisture content and surface water amounts. Finally, these fields are aggregated back to the coarser grid of the LSM by simple averaging and an updated set of weighting factors is calculated accordingly.

It is highlighted that the simulation of river discharge with WRF-Hydro-tag would require to activate an additional routing module in the river channels. Several studies have assessed the skill of WRF-Hydro in reproducing observed discharge (e.g., Camera et al., 2020; Fersch et al., 2020; Li et al., 2020; Senatore et al., 2020). In this study, the focus is on the contribution of lateral terrestrial water flow to the atmospheric branch of the hydrologic cycle, and no channel routing is considered.

With respect to model parameter calibration, it is recognized that for a fair comparison of model performances with a simulation including lateral terrestrial water flow, the Noah-MP parameters of a simulation with purely vertical terrestrial water flow should probably be calibrated differently in order to compensate for the effect of lateral

terrestrial water flow (e.g., Arnault, Wagner, et al., 2016; Fersch et al., 2020; Rummler et al., 2019). However, the aim of this study is to compare simulations with and without lateral terrestrial water flow in order to extract the effect of lateral terrestrial water flow on precipitation. In order to extract this effect without ambiguity, it is chosen to keep the default values of the Noah-MP parameters for all simulations. It is acknowledged that the estimation of the uncertainty in such a model comparison would benefit from the consideration of several plausible Noah-MP parameters sets in an ensemble of simulations. It is noted that the following uncertainty analysis is limited to the atmospheric part. Other potential sources of uncertainty, such as from the land surface part, are likely to further increase uncertainty ranges.

The same model outputs are used for the WRF-tag and WRF-Hydro-tag simulations, except for the surface runoff. The WRF-tag surface runoff is computed as the surface infiltration excess (Schaake et al., 1996), whereas the WRF-Hydro-tag surface runoff is computed as the surface water which flows out of a grid cell, either through overland flow or through river channel inflow (Arnault et al., 2019). The saved model outputs include land surface variables and vertically-integrated terms of the total and tagged atmospheric water budgets, saved at an hourly time interval.

2.4 | Ensemble generation strategy

It is well known that a numerical simulation of atmospheric processes contains a part of randomness (e.g., Lorenz, 1969). Accordingly, the difference in precipitation between WRF-tag and WRF-Hydro-tag simulations may be due to both lateral terrestrial water flow and modelled atmospheric randomness. Therefore, the estimation of the effect of modelled atmospheric randomness is crucial in order to extract the real contribution of lateral terrestrial water flow to the precipitation difference between WRF-tag and WRF-Hydro-tag simulations. Such a modelled atmospheric randomness effect is usually assessed with simulations' ensembles (e.g., Errico et al., 2002; Hohenegger et al., 2008).

The WRF model provides a tool to generate such an ensemble based on the stochastic kinetic energy backscatter scheme (SKEBS, Berner et al., 2009; Shutts, 2005). SKEBS allows to slightly perturb the wind, temperature and geopotential variables with a random noise through the model run, in order to represent atmospheric random variability.

For the purpose of disentangling the respective effects of modelled atmospheric randomness and lateral terrestrial water flow on precipitation, an ensemble of 30 WRF-tag simulations and 30 WRF-Hydro-tag simulations is generated with 30 different realizations of the random noise in SKEBS, for both Europe and West Africa, and for the study period from June to September 2008. The initial condition of the WRF-tag and WRF-Hydro-tag sub-ensemble members, that is on 1 June 2008, is obtained with WRF-tag and WRF-Hydro-tag single runs for the spinup period from January to May 2008.

2.5 | Convergence criteria

The aim of generating an ensemble mean is to reduce the influence of modelled atmospheric randomness (e.g., Hohenegger et al., 2008). Still, it is not known which is the minimal ensemble size required so that differences between WRF-tag and WRF-Hydro-tag sub-ensemble means would be mainly the effect of lateral terrestrial water flow. In order to quantify the influence of modelled atmospheric randomness on ensemble-mean difference in precipitation, we consider the following convergence criterion $c^{spatialpattern}$ (−) as a function of ensemble size n:

$$c^{spatialpattern}(n) = \sum_{(i,j)\,\in\,land} \left(\frac{\frac{1}{nb(n)} \sum_{p=1}^{nb(n)} \left(\frac{1}{n} \sum_{k\,\in\,\mathrm{E}(n,p)} P_{WH}^{i,j,k} - P_{W}^{i,j,k} \right)}{\max\limits_{1\,\le\,p\,\le\,nb(n)} \left(\frac{1}{n} \sum\limits_{k\,\in\,\mathrm{E}(n,p)} P_{WH}^{i,j,k} - P_{W}^{i,j,k} \right) - \min\limits_{1\,\le\,p\,\le\,nb(n)} \left(\frac{1}{n} \sum\limits_{k\,\in\,\mathrm{E}(n,p)} P_{WH}^{i,j,k} - P_{W}^{i,j,k} \right)} \right) \quad (1)$$

$c^{spatialpattern}$ is the spatially-averaged signal-to-noise ratio of ensemble-mean differences in precipitation between WRF-tag and WRF-Hydro-tag sub-ensembles, the signal-to-noise ratio being here defined as the ratio between the ensemble mean and the ensemble spread, as an adaptation from Laux et al. (2017). $P_{W}^{i,j,k}$ (m/s) and $P_{WH}^{i,j,k}$ (m/s) are the precipitation rates at grid point i, j for the WRF-tag sub-ensemble member k and the WRF-Hydro-tag sub-ensemble member k, respectively, temporally averaged for the study period. $\mathrm{E}(n, p)$ refers to the list of indexes of the n members of sub-ensemble p, these n members being randomly selected between 1 and the full ensemble size n_{ENS}, n_{ENS} being equal to 30 in this case. The index p varies between 1 and $nb(n) = \frac{n_{ENS}!}{n!(n_{ENS}!-n!)}$, that is the number of possible combinations of sub-ensembles of size n within the full ensemble. Technically, this number of sub-ensemble combinations is truncated at 1 000 000 for computational reasons. By definition, $c^{spatialpattern}$ can only be calculated for n between 1 and $n_{ENS} - 1$. Furthermore, the number of sub-ensemble combinations for the calculation of $c^{spatialpattern}$ is much smaller for small and large values of n than for middle values of n, which implies an overestimation of the signal-to-noise ratio especially for n values close to $n_{ENS} - 1$. The aim of $c^{spatialpattern}$ is to measure the dependency of the spatial differences between WRF-tag and WRF-Hydro-tag sub-ensemble means of precipitation to n. For sufficiently large n and n_{ENS}, the effect of modelled

atmospheric randomness on these spatial differences is expected to become negligible and $c^{spatialpattern}$ to reach values beyond 1.

The influence of modelled atmospheric randomness on ensemble-mean results is assessed with the following convergence criterion c^{mean} (−):

$$c^{mean}(n) = \frac{\frac{1}{nb(n)}\sum_{p=1}^{nb(n)}\left(\sum_{(i,j)\in land}\left(\frac{1}{n}\sum_{k\in E(n,p)}P_{WH}^{i,j,k} - P_{W}^{i,j,k}\right)\right)}{\max_{1\le p\le nb(n)}\left(\sum_{(i,j)\in land}\left(\frac{1}{n}\sum_{k\in E(n,p)}P_{WH}^{i,j,k} - P_{W}^{i,j,k}\right)\right) - \min_{1\le p\le nb(n)}\left(\sum_{(i,j)\in land}\left(\frac{1}{n}\sum_{k\in E(n,p)}P_{WH}^{i,j,k} - P_{W}^{i,j,k}\right)\right)} \quad (2)$$

c^{mean} is the signal-to-noise ratio of the spatially-averaged ensemble-mean differences in precipitation between WRF-tag and WRF-Hydro-tag sub-ensembles. In comparison to $c^{spatialpattern}$, c^{mean} measures the dependency of the spatially-average difference between WRF-tag and WRF-Hydro-tag sub-ensemble means of precipitation to n. As for $c^{spatialpattern}$, the effect of modelled atmospheric randomness is also expected to become negligible and c^{mean} to reach values beyond 1 for growing n.

Both $c^{spatialpattern}$ and c^{mean} are used to evaluate the contribution of modelled atmospheric randomness to the difference between WRF-tag and WRF-Hydro-tag sub-ensemble means, and better quantify the overall contribution of lateral terrestrial water flow to summer-mean precipitation.

2.6 | Ensemble-mean differences

The role of lateral terrestrial water flow in the summer-mean hydrologic cycle can be assessed by comparing ensemble means of water fluxes between the WRF-tag and WRF-Hydro-tag sub-ensembles, temporally averaged for the study period from June to September 2008. In the following, the water fluxes are computed as rates. The selected measures are the ensemble-mean differences in surface runoff ΔR (m/s), land surface evaporation ΔE (m/s), atmospheric water content ΔW (m), total precipitation ΔP (m/s), precipitation originating from land surface evaporation ΔP_{land} (m/s), precipitation originating from remote water sources ΔP_{remote} (m/s), and land precipitation recycling ratio $\Delta\rho$ (%), defined as follows:

$$\Delta R = R_{ENS,WH} - R_{ENS,W} \quad (3)$$

$$\Delta E = E_{ENS,WH} - E_{ENS,W} \quad (4)$$

$$\Delta W = W_{ENS,WH} - W_{ENS,W} \quad (5)$$

$$\Delta P = P_{ENS,WH} - P_{ENS,W} \quad (6)$$

$$\Delta P_{land} = P_{ENS,WH}^{tag} - P_{ENS,W}^{tag} \quad (7)$$

$$\Delta P_{remote} = (P_{ENS,WH} - P_{ENS,W}) - \left(P_{ENS,WH}^{tag} - P_{ENS,W}^{tag}\right) \quad (8)$$

$$\Delta\rho = \underbrace{100\frac{P_{ENS,WH}^{tag}}{P_{ENS,WH}}}_{\rho_{ENS,WH}} - \underbrace{100\frac{P_{ENS,W}^{tag}}{P_{ENS,W}}}_{\rho_{ENS,W}} \quad (9)$$

Subscripts *ENS*, *W* and *ENS*, *WH* stand for WRF-tag and WRF-Hydro-tag sub-ensemble means. $R_{ENS,W}$ (m/s), $R_{ENS,WH}$ (m/s), $E_{ENS,W}$ (m/s), $E_{ENS,WH}$ (m/s), $W_{ENS,W}$ (m), $W_{ENS,WH}$ (m), $P_{ENS,W}$ (m/s), $P_{ENS,WH}$ (m/s), $P_{ENS,W}^{tag}$, and $P_{ENS,WH}^{tag}$ (m/s) are sub-ensemble means of surface runoff, land surface evaporation, atmospheric water content, precipitation, and tagged precipitation, all computed with the 30 available members and temporally averaged for the study period.

ΔR, ΔE, ΔW, ΔP, ΔP_{land}, ΔP_{remote}, and $\Delta\rho$ quantify the impact of lateral terrestrial water flow on the summer-mean terrestrial and atmospheric branches of the hydrologic cycle. More particularly, ΔP_{land} represents a direct atmospheric water pathway linking a lateral terrestrial water flow-induced change in land surface evaporation with a change in precipitation. ΔP_{remote} is the fraction of the difference in precipitation induced by lateral terrestrial water flow which does not originate from land surface evaporation, but instead originates from sea surface evaporation or from atmospheric water vapour entering the simulations' domain at the lateral boundaries. Therefore, ΔP_{remote} represents an indirect atmospheric water pathway linking a lateral terrestrial water flow-induced change in land surface evaporation with a change in precipitation through remote water sources contribution. Finally, $\Delta\rho$ represents the impact of lateral terrestrial water flow on the amount of land precipitation recycling, which is a measure of the coupling strength between land and atmosphere at continental-scale (e.g., Brubaker et al., 1993).

2.7 | Normalized ensemble spread

Following Keil et al. (2014) and Arnault et al. (2018), the impact of lateral terrestrial water flow on modelled precipitation uncertainty is evaluated with the normalized ensemble spread of daily precipitation. The method is to compare the normalized ensemble spreads $S_{ENS,W}^{daily}$ (−) and $S_{ENS,WH}^{daily}$ (−) from the WRF-tag and WRF-Hydro-tag sub-ensembles, defined as:

$$S_{ENS,W}^{daily} = \frac{1}{P_{ENS,W}^{daily}}\sqrt{\frac{1}{n_{ENS}-1}\sum_{k=1}^{n_{ENS}}\left(P_{W}^{daily,k} - P_{ENS,W}^{daily}\right)^2}$$

$$S_{ENS,WH}^{daily} = \frac{1}{P_{ENS,WH}^{daily}} \sqrt{\frac{1}{n_{ENS}-1} \sum_{k=1}^{n_{ENS}} \left(P_{WH}^{daily,k} - P_{ENS,WH}^{daily} \right)^2} \quad (10)$$

$P_{W}^{daily,k}$ (m/s) and $P_{WH}^{daily,k}$ (m/s) are the daily precipitation rates for the WRF-tag ensemble member k and the WRF-Hydro-tag ensemble member k, respectively. $P_{ENS,W}^{daily,}$ (m/s) and $P_{ENS,WH}^{daily,}$ (m/s) are the WRF-tag and WRF-Hydro-tag sub-ensemble means of daily precipitation rate, respectively, and n_{ENS} is the full ensemble size. $S_{ENS,W}^{daily}$ and $S_{ENS,WH}^{daily}$ are computed for the grid cells receiving an ensemble-mean precipitation larger than 1 mm/day, and can be visualized as maps. The summer-mean impact of lateral terrestrial water on modelled precipitation uncertainty is assessed with $S_{ENS,W}$ (−) and $S_{ENS,WH}$ (−), that are the values of $S_{ENS,W}^{daily}$ and $S_{ENS,WH}^{daily}$ temporally averaged for the study period, and with ΔS (%), that is the normalized difference between $S_{ENS,W}$ and $S_{ENS,WH}$.

2.8 | Hydro-specific land precipitation recycling difference

In the case of Central Europe, Arnault et al. (2018) found that lateral terrestrial water flow noticeably increases modelled precipitation uncertainty when local processes dominate the weather regime and moist convection initiation is favoured by enhanced surface flux heterogeneity, which in fact characterizes an enhanced land – atmosphere coupling situation.

In this study, the relationship between the strength of the land – atmosphere coupling and the impact of lateral terrestrial water flow on modelled precipitation uncertainty is evaluated with the so-called hydro-specific land precipitation recycling difference $\Delta\rho^{hydro}$ (%), calculated as the difference in ensemble-mean daily land precipitation recycling between the days when $S_{ENS,WH}^{daily}$ exceeds $S_{ENS,W}^{daily}$ by more than 20%, and the days when $S_{ENS,W}^{daily}$ exceeds $S_{ENS,WH}^{daily}$ by more than 20%. This threshold of 20% is arbitrarily chosen and was originally proposed by Arnault et al. (2018). This threshold does not need to be precisely set to 20%, as for example very similar results to those presented in this study have been obtained with a threshold of 15% (not shown). The formulation of $\Delta\rho^{hydro}$ is:

$$\Delta\rho^{hydro} = \frac{\sum_{days} 100 \frac{P_{ENS}^{tag,daily}}{P_{ENS}^{daily}} \cdot H\left(S_{ENS,WH}^{daily} - 1.2 S_{ENS,W}^{daily} \right)}{\sum_{days} H\left(S_{ENS,WH}^{daily} - 1.2 S_{ENS,W}^{daily} \right)} - \frac{\sum_{days} 100 \frac{P_{ENS}^{tag,daily}}{P_{ENS}^{daily}} \cdot H\left(S_{ENS,W}^{daily} - 1.2 S_{ENS,WH}^{daily} \right)}{\sum_{days} H\left(S_{ENS,H}^{daily} - 1.2 S_{ENS,WH}^{daily} \right)} \quad (11)$$

P_{ENS}^{daily} is the ensemble mean of daily precipitation and $P_{ENS}^{tag,daily}$ is the ensemble mean of daily tagged precipitation. H is the Heaviside function and $H\left(S_{ENS,WH}^{daily} - 1.2 S_{ENS,W}^{daily} \right)$ and $H\left(S_{ENS,W}^{daily} - 1.2 S_{ENS,WH}^{daily} \right)$ are two Boolean numbers which are used to assess for which days the above conditions on $S_{ENS,W}^{daily}$ and $S_{ENS,WH}^{daily}$ values are met. $\Delta\rho^{hydro}$ quantifies the relative strength of land – atmosphere coupling for the days when lateral terrestrial water flow noticeably increases modelled precipitation uncertainty.

2.9 | Hydro-specific atmospheric water content difference

Moist convection is sensitive to environmental humidity (e.g., Derbyshire et al., 2004). Therefore, the impact of lateral terrestrial water flow on modelled precipitation uncertainty may be related to the potential increase in atmospheric water content induced by lateral terrestrial water flow. This relationship is evaluated with the so-called hydro-specific atmospheric water content difference ΔW^{hydro} (m), calculated by subtracting (1) the difference between the WRF-tag and WRF-Hydro-tag sub-ensemble mean daily atmospheric water content for the days when $S_{ENS,W}^{daily}$ exceeds $S_{ENS,WH}^{daily}$ by more than 20%, to (2) the difference between the WRF-tag and WRF-Hydro-tag sub-ensemble mean daily atmospheric water content for the days when $S_{ENS,WH}^{daily}$ exceeds $S_{ENS,W}^{daily}$ by more than 20%. The formulation of ΔW^{hydro} is:

$$\Delta W^{hydro} = \frac{\sum_{days} \left(W_{ENS,WH}^{daily} - W_{ENS,W}^{daily} \right) \cdot H\left(S_{ENS,WH}^{daily} - 1.2 S_{ENS,W}^{daily} \right)}{\sum_{days} H\left(S_{ENS,WH}^{daily} - 1.2 S_{ENS,W}^{daily} \right)} - \frac{\sum_{days} \left(W_{ENS,WH}^{daily} - W_{ENS,W}^{daily} \right) \cdot H\left(S_{ENS,W}^{daily} - 1.2 S_{ENS,WH}^{daily} \right)}{\sum_{days} H\left(S_{ENS,W}^{daily} - 1.2 S_{ENS,WH}^{daily} \right)} \quad (12)$$

$W_{ENS,W}^{daily}$ and $W_{ENS,WH}^{daily}$ are the WRF-tag and WRF-Hydro-tag sub-ensemble means of daily atmospheric water content. ΔW^{hydro} quantifies the relative intensity of the atmospheric water content perturbation induced by lateral terrestrial water flow for the days when lateral terrestrial water flow noticeably increases modelled precipitation uncertainty.

3 | RESULTS AND DISCUSSIONS

3.1 | Comparison to observation

The skill of WRF-tag and WRF-Hydro-tag is evaluated for the two study regions by comparing ensemble means of land surface evaporation and precipitation to gridded datasets, temporally averaged for the study period in Figures 2 and 3.

For Europe, the land surface evaporation is generally underestimated, except in the Alpine region. The land surface evaporation bias is comparable in magnitude to climate simulations' results for Europe in summer (Knist et al., 2017). Precipitation is much closer to the observational dataset, except for the southern parts where the observed low precipitation rates are much overestimated. Comparable precipitation biases have been obtained with climate simulations for Europe in summer (Prein et al., 2016).

For West Africa the land surface evaporation is close to the observational dataset (as in Arnault, Wagner, et al., 2016), except in

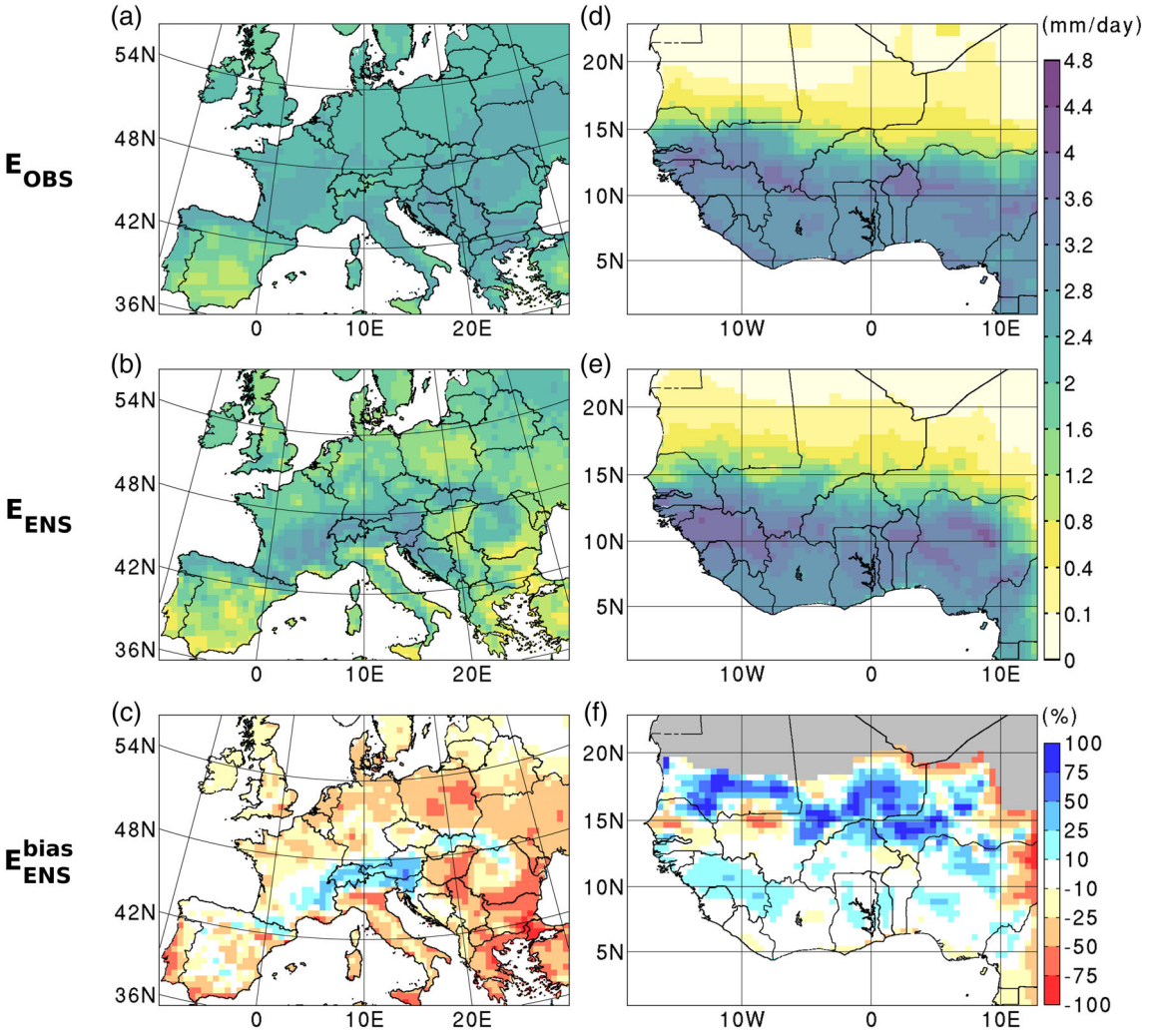

FIGURE 2 (a,b) Maps of observational land surface evaporation E_{OBS} and ensemble-mean land surface evaporation E_{ENS} temporally averaged for the 4-month period from June to September 2008 and given in mm/day, for Europe. (c) Ensemble-mean bias E_{ENS}^{bias} given in %. (d–f) As in (a–c), except for West Africa. The areas with temporally averaged E_{ENS} or E_{OBS} lower than 0.1 mm/day are shaded in grey in the bias maps. In all panels the data has been resampled on a grid with a 50 km grid spacing for visualization purpose. A similar resampling is applied to all maps shown in the following of this study

the northern part of the Sahel between 15°N and 20°N where observed low rates in land surface evaporation are remarkably overestimated. The overall bias in precipitation for West Africa is also quite low, which confirms the potential of explicitly resolved moist convection in realistically representing West African monsoonal rainfall (e.g., Marsham et al., 2013).

Quantitatively, the spatially averaged bias in land surface evaporation is −24% for Europe and 6% for West Africa, whereas the spatially averaged bias in precipitation is −0.5% for Europe and −4% for West Africa. The relatively small precipitation biases are related to the fact that much larger biases of the order of ±50% cancel after spatial averaging. Still, this relatively good agreement between ensemble-mean results and observations suggests that the model setup is suitable for representing the summer-mean characteristics of the land – atmosphere system in both Europe and West Africa.

It is noted that single ensemble members may have a better spatially averaged bias in precipitation in comparison to the ensemble mean, although there is a large spread among ensemble members with bias values ranging from −6% to 7% for Europe, and from −11% to 4% for West Africa. Nevertheless, the spatial root mean square deviation of the precipitation bias from the ensemble mean is generally lower than that from each ensemble member, with a relative difference ranging from −34% to 2%. This confirms that the ensemble mean is suitable for smoothing random errors in modelled precipitation (e.g., Hohenegger et al., 2008).

Daily time series of land-average precipitation sums in Figure 4 demonstrate that the model setup is able to produce a realistic history of the daily precipitation events having occurred in Europe and West Africa between June and September 2008. In particular, the correlation coefficient between modelled and observational

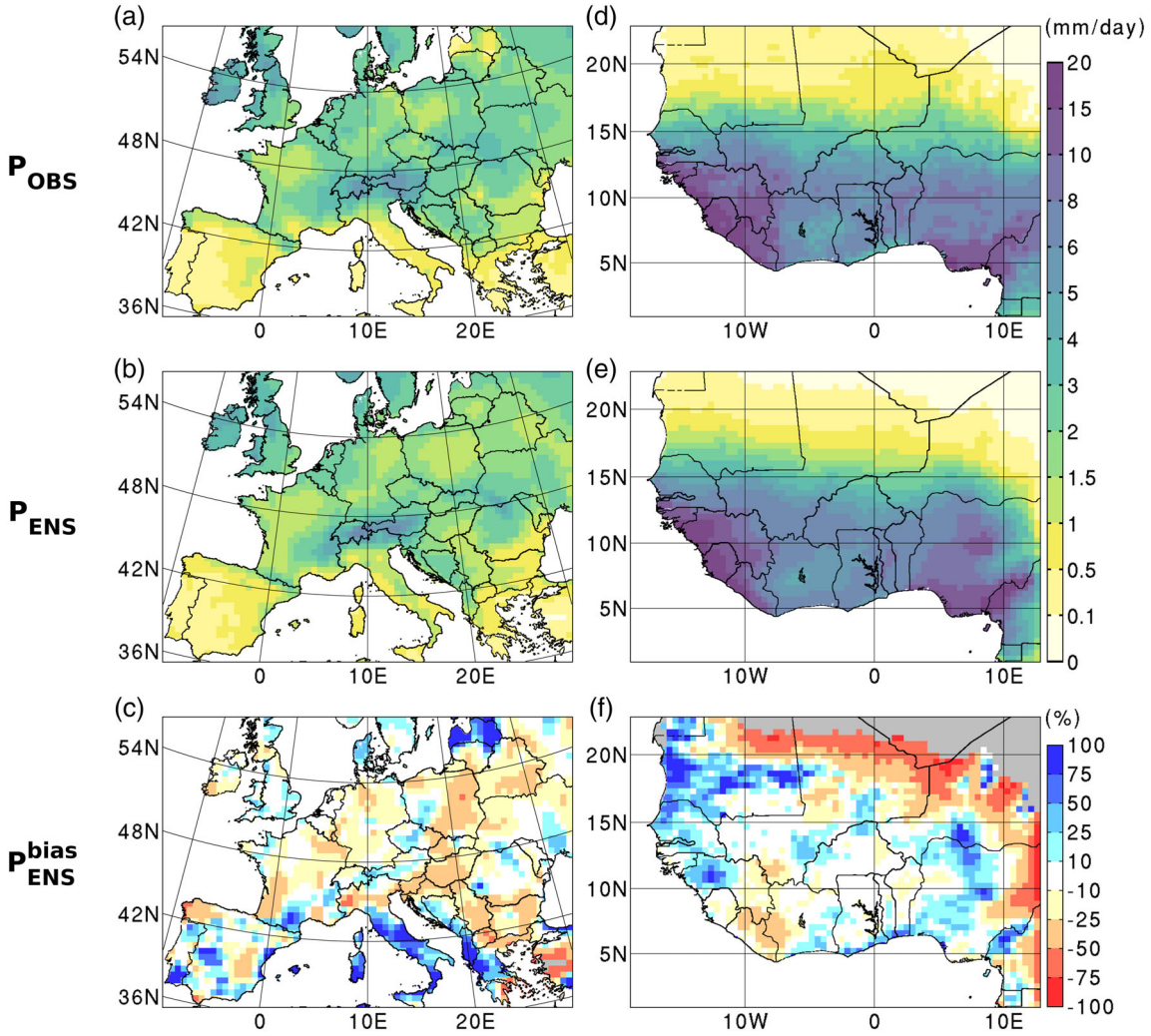

FIGURE 3 (a,b) Maps of observational precipitation P_{OBS} and ensemble-mean precipitation P_{ENS} temporally averaged for the 4-month period from June to September 2008 and given in mm/day, for Europe. (c) Ensemble-mean bias P_{ENS}^{bias} given in %. (d–f) As in (a–c), except for West Africa. The areas with temporally averaged P_{ENS} or P_{OBS} lower than 0.1 mm/day are shaded in grey in the bias maps

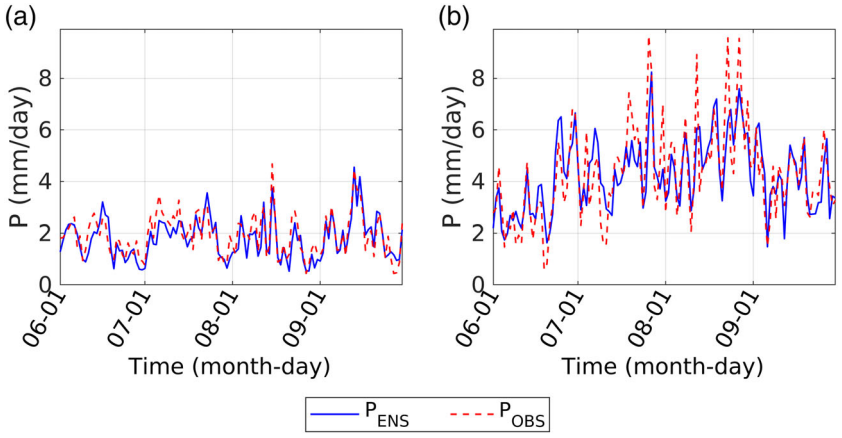

FIGURE 4 Daily time series of ensemble-mean and observed precipitation, P_{ENS} and P_{OBS}, spatially averaged over the land in the simulation's domain and displayed from June to September 2008 for (a) Europe and (b) West Africa

precipitation time series is 0.84 for Europe, and 0.78 for West Africa. This suggests that the model setup is also suitable for representing the daily variability of the land – atmosphere system in both Europe and West Africa.

3.2 | Atmospheric randomness

The effect of modelled atmospheric randomness on mean-ensemble results is evaluated for the case of the ensemble-mean difference in

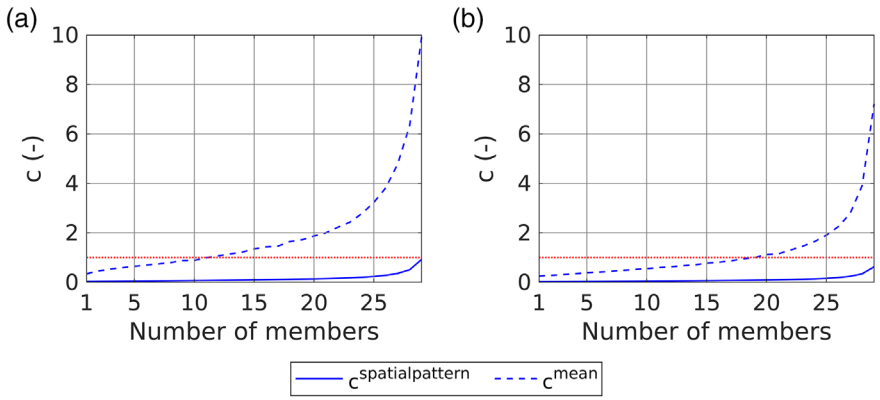

FIGURE 5 Convergence criteria $c^{spattialpattern}$ and c^{mean} plotted as a function of ensemble size for (a) Europe and (b) West Africa. The threshold of 1 is indicated by the dotted red line. The threshold of 1 is indicated by the dotted red line. For $c^{spattialpattern}$ above 1, the effect of lateral terrestrial water flow on the spatial patterns of the difference between the WRF-tag and WRF-Hydro-tag ensemble-means is larger than the atmospheric random variability. For c^{mean} above 1, the effect of the lateral terrestrial water flow on the spatially-averaged difference between the WRF-tag and WRF-Hydro-tag ensemble-means is larger than the atmospheric random variability

precipitation ΔP, using the convergence criteria $c^{spatialpattern}$ and c^{mean} displayed in Figure 5. $c^{spatialpattern}$ confirms that the dependency of ΔP's spatial variability to modelled atmospheric randomness decreases with the size of the ensemble. However, for n equal to $n_{ENS}-1$, $c^{spatialpattern}$ hardly reaches 0.9 in the case of Europe, and 0.6 in the case of West Africa, which implies that the spatial features of ΔP are partially related to modelled atmospheric randomness, and that a larger ensemble size would be required in order to isolate the pure effect of lateral terrestrial water flow on the spatial distribution of precipitation. Due to interdependency between water compartments in the hydrologic cycle, this result suggests that the spatial features of ΔR, ΔE, ΔW, ΔP_{land}, ΔP_{remote}, and $\Delta\rho$ are also partially related to modelled atmospheric randomness.

c^{mean} is an increasing function of n as $c^{spatialpattern}$ with values much above those of $c^{spatialpattern}$. Particularly, c^{mean} reaches 1 for an ensemble size of 12 in case of Europe, and for an ensemble size of 20 in the case of West Africa. The lower signal-to-noise ratio in the case of West Africa is related to the large atmospheric random variability associated with tropical convection (e.g., Peters et al., 2013). This indicates that modelled atmospheric randomness has a major impact on spatially-averaged mean differences of precipitation when the ensemble size is small, especially for West Africa, and that this impact can be much reduced for a sufficiently large ensemble size, like 30 in this case. Accordingly, spatially averaged values of the above-mentioned ensemble-mean differences can be used to isolate the effect of lateral terrestrial water flow on the spatially averaged hydrologic cycle at continental scale.

The model uncertainty associated with these ensemble-mean differences is evaluated with the range of all possible sub-ensemble-mean differences using a slightly reduced sub-ensemble size, arbitrarily set to 27, which corresponds to 4060 combinations. A lower sub-ensemble size would increase the computational time of the uncertainty calculation, and would also increase the value of the calculated uncertainty, which may not be a fair estimation of the uncertainty related to the full-size ensemble-mean differences. In the following, this uncertainty is indicated in parenthesis of each ensemble-mean difference value, such as in Table 1.

TABLE 1 Normalized ensemble-mean differences in surface runoff ($\Delta R/P_{ENS}$), land surface evaporation ($\Delta E/P_{ENS}$), precipitation originating from land surface evaporation ($\Delta P_{land}/P_{ENS}$), and precipitation originating from remote water sources ($\Delta P_{remote}/P_{ENS}$), spatially averaged for the land in the simulation's domain for Europe and West Africa and given in %

	Europe	West Africa
$\Delta R/P_{ENS}$	−2.6 (±0.1) %	−6.9 (±0.1) %
$\Delta E/P_{ENS}$	3.5 (±0.1) %	2.2 (±0.1) %
$\Delta P_{land}/P_{ENS}$	0.8 (±0.1) %	1.0 (±0.1) %
$\Delta P_{remote}/P_{ENS}$	0.8 (±0.2) %	−0.2 (±0.2) %

Note: The uncertainty range, which is provided in parenthesis, is derived from all the combinations of sub-ensemble-mean differences with an ensemble subset of 27 members out of the 30 members available.

3.3 | Surface runoff

As shown by ΔR in Figure 6, WRF-Hydro-tag produces more surface runoff than WRF-tag in mountainous areas, such as the Scottish Highlands, Pyrenees, Massif Central, Alps and the Carpathian Mountains in Europe, and Fouta Djallon, Jos Plateau and Adamawa Plateau in West Africa (see locations of these mountain ranges in Figure 1). The enhanced mountainous surface runoff generation in WRF-Hydro-tag is related to steep topography gradients which favour the exfiltration from saturated soil columns (e.g., Arnault et al., 2019).

WRF-Hydro-tag produces less surface runoff than WRF-tag in areas where the re-infiltration of infiltration excess occurs more frequently than channel inflow, in relation to either moderate terrain or

reduced precipitation amounts. This latter effect is well illustrated with the case of southern Europe, such as the Balkan Mountains, where topography gradients are relatively steep but the particularly low precipitation amounts during the study period weaken the surface runoff generation in WRF-Hydro-tag.

3.4 | Land surface evaporation

The decrease in surface runoff induced by lateral terrestrial water flow is associated with an increase in soil water storage and in land surface evaporation, which is a well-documented effect (e.g., Arnault et al., 2018; Arnault, Wagner, et al., 2016; Fersch et al., 2020; Rummler et al., 2019; Sulis et al., 2018; Zhang et al., 2019) and is mostly verified in this case, as shown by ΔE in Figure 7. Still, there are few areas in Figure 7 where WRF-Hydro-tag produces less land surface evaporation in comparison to WRF-tag, such as the above-described mountainous areas where WRF-Hydro-tag produces more surface runoff and less soil water storage, but also the areas where WRF-Hydro-tag produces less precipitation in comparison to WRF-tag.

As illustrated in Table 1, the decrease in surface runoff in Europe is overbalanced by an increase in land surface evaporation, which demonstrates that a soil moisture-limited evaporation regime (e.g., Dirmeyer et al., 2012) is at stake in this region during the study period. In comparison, the decrease in surface runoff in West Africa is much larger although the increase in land surface evaporation is much smaller. Indeed, during the study period West Africa receives much larger precipitation amounts than Europe, which reduces the root zone transit times (Sprenger et al., 2016) and enhances percolation. This suggests that in comparison to Europe during the study period, the soil columns in West Africa are much closer to saturation and the evaporation regime is less soil moisture-limited.

3.5 | Atmospheric water content

As shown by $W_{ENS,W}$ in Figure 8, the atmosphere in tropical West Africa is much more moist than in the mid-latitude Europe during the study period, which is expected. ΔW in Figure 8 further shows that the increase in surface evaporation induced by lateral terrestrial water flow mostly wets the entire atmosphere in both study regions.

In Europe, there is a blocking effect south of the Alps and around the Carpathian Mountains which enhances the accumulation of atmospheric water content originating from lateral terrestrial water flow. In West Africa, there is an enhanced accumulation of atmospheric water content north of 12°N. This accumulation is related to the south-westerly monsoonal flow pushing low-level

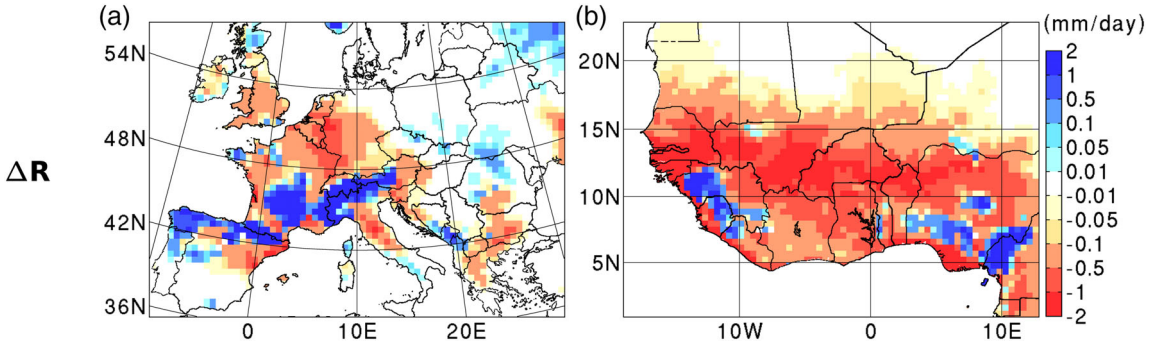

FIGURE 6 Maps of the ensemble-mean difference in surface runoff ΔR temporally averaged from June to September 2008 for (a) Europe and (b) West Africa, given in mm/day

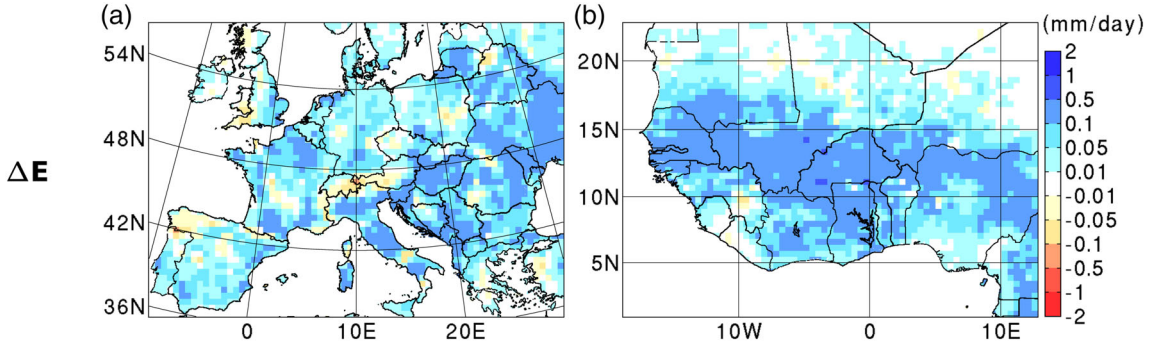

FIGURE 7 Maps of the ensemble-mean difference in surface evaporation ΔE temporally averaged from June to September 2008 for (a) Europe and (b) West Africa, given in mm/day

moisture towards the inland area, and the monsoonal squall lines north of 12°N (Laing et al., 2008) which slow down the progression of the enhanced atmospheric water content by partially converting it into precipitation.

3.6 | Atmospheric water pathways

The direct and indirect pathways of the atmospheric water which becomes precipitation are evaluated with ΔP_{land} and ΔP_{remote} in Figure 9.

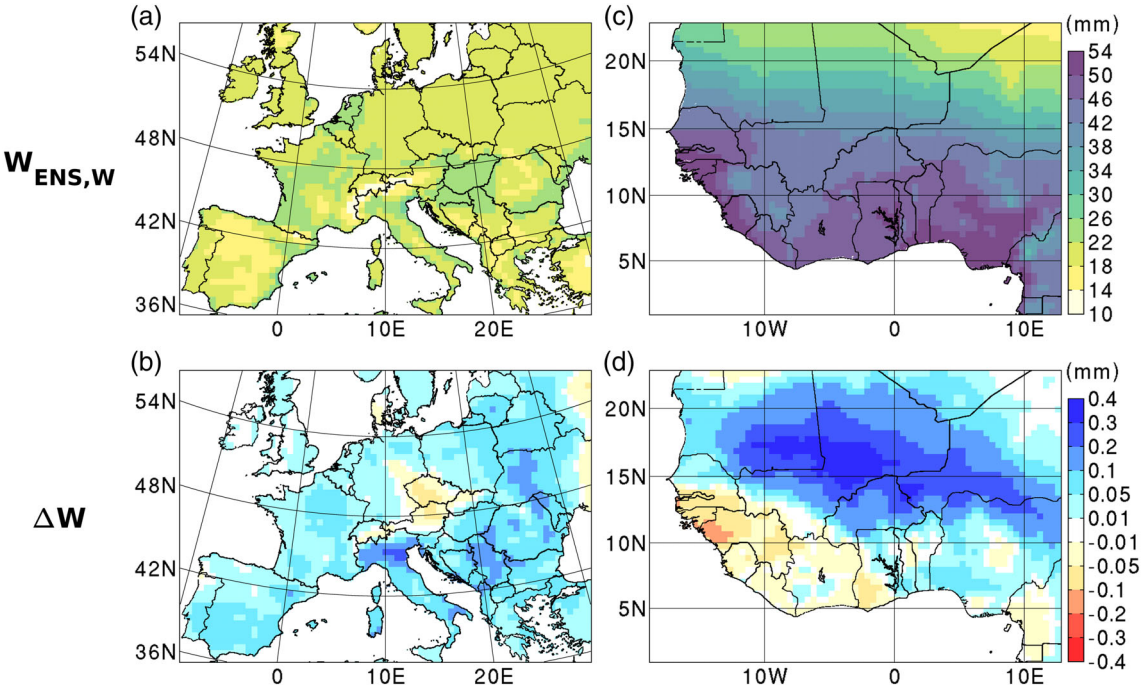

FIGURE 8 (a,b) Maps of (a) WRF-tag sub-ensemble mean of atmospheric water $W_{ENS,W}$ and (b) ensemble-mean difference in atmospheric water ΔW, both temporally averaged from June to September 2008 for Europe and given in mm. (c,d) As in (a,b), except for West Africa

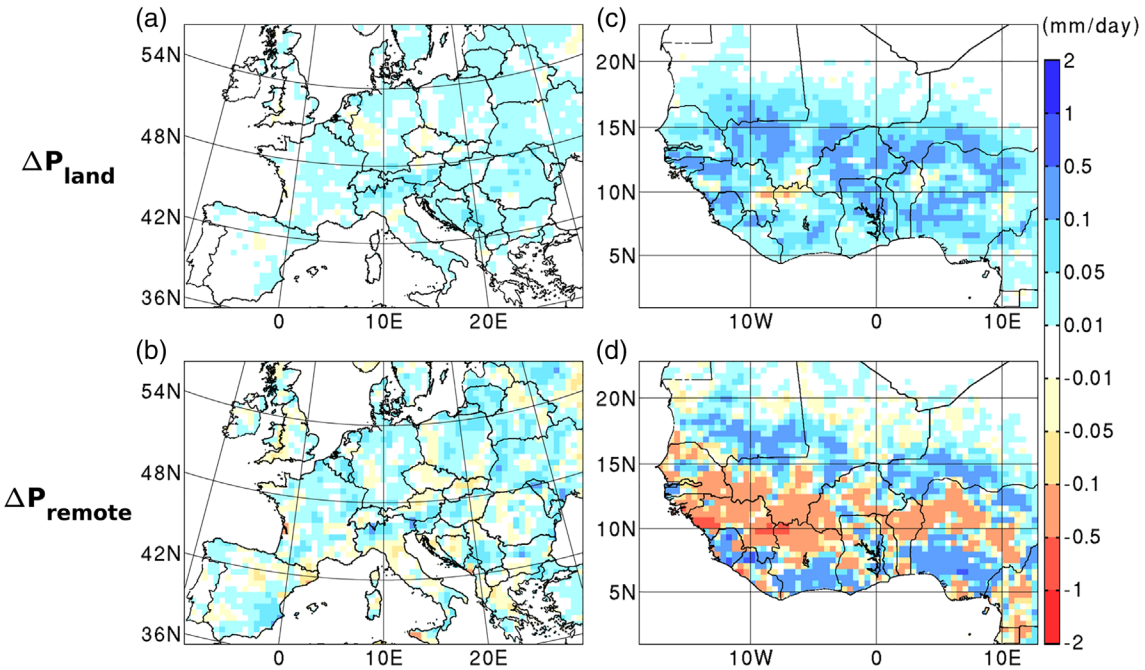

FIGURE 9 (a,b) Maps of ensemble-mean differences in (a) precipitation originating from land surface evaporation ΔP_{land} and (b) precipitation originating from remote water sources ΔP_{remote}, both temporally averaged from June to September 2008 for Europe and given in mm/day. (c,d) As in (a,b), except for West Africa

The dominant positive areas in ΔP_{land} for both Europe and West Africa demonstrate that in both study regions the soils are sufficiently wet in order to support a summer-mean positive soil moisture – precipitation feedback (Hsu et al., 2017), and ensure that the soil moisture-increase induced by lateral terrestrial water flow leads to an increase in the summer-mean precipitation.

In comparison to ΔP_{land}, ΔP_{remote} features much more spatial variability, which is assumed to be partially the effect of model atmospheric randomness. In the case of Europe, as shown in Table 1, spatially averaged values of ΔP_{land} and ΔP_{remote} are close, which means that lateral terrestrial water flow contributes to precipitation also through an indirect pathway linking remote water sources to a change in precipitation. A possible mechanism to explain this would be that in average the increase in land surface evaporation increases the size of the precipitating systems, which makes them more efficient in collecting water from remote sources and generating more precipitation.

ΔP_{remote} spatial variability in West Africa is enhanced in comparison to Europe. The above-described indirect pathway of precipitation enhancement occurs north of 12°N in West Africa. An opposite effect can be seen south of 12°N, where an enhancement of the land surface evaporation contribution to precipitation is associated with a decrease of the remote water contribution to precipitation. However, the ensemble size is not large enough to guarantee that these spatial distribution characteristics of the indirect pathway in West Africa are not triggered by modelled atmospheric randomness.

3.7 | Land precipitation recycling ratio

As shown by $\rho_{ENS,W}$ in Figure 10, land precipitation recycling in Europe is larger in Central Europe, with maxima up to 30% and a spatially averaged value around 16%, which is in the range of published continental precipitation recycling estimates (e.g., Brubaker et al., 1993; van der Ent et al., 2010). For West Africa, land precipitation recycling is also larger towards the inland area, with maxima up to 30% and a spatially averaged value around 19%. The land area of the simulation's domain has a size of about 6 000 000 km^2. In comparison, Arnault, Knoche, et al. (2016) found a regional precipitation recycling of about 12% for a squared 1 000 000 km^2 area in West Africa. Such a scaling effect is expected (e.g., Trenberth, 1999).

Lateral terrestrial water flow increases land precipitation recycling in most regions of Europe and West Africa, as shown by $\Delta\rho$ in Figure 10. In West Africa, a relative increase in land precipitation recycling by up to 10% is found north of 12°N, which suggests an enhanced sensitivity of monsoonal squall lines to lateral terrestrial water flow. Overall, lateral terrestrial water flow increases the spatially averaged value of the land precipitation recycling ratio from 15.9 (±0.1)% to 16.5 (±0.1)% in Europe, which corresponds to a relative increase of 3.6 (±0.2)%, and from 18.9 (±0.1)% to 20.0 (±0.1)% in West Africa, which corresponds to a relative increase of 5.6 (±0.2)%, the uncertainty ranges being deduced from all combinations of subsets of 27 members out of 30 as detailed above. This result means that lateral terrestrial water flow enhances the strength of the land –

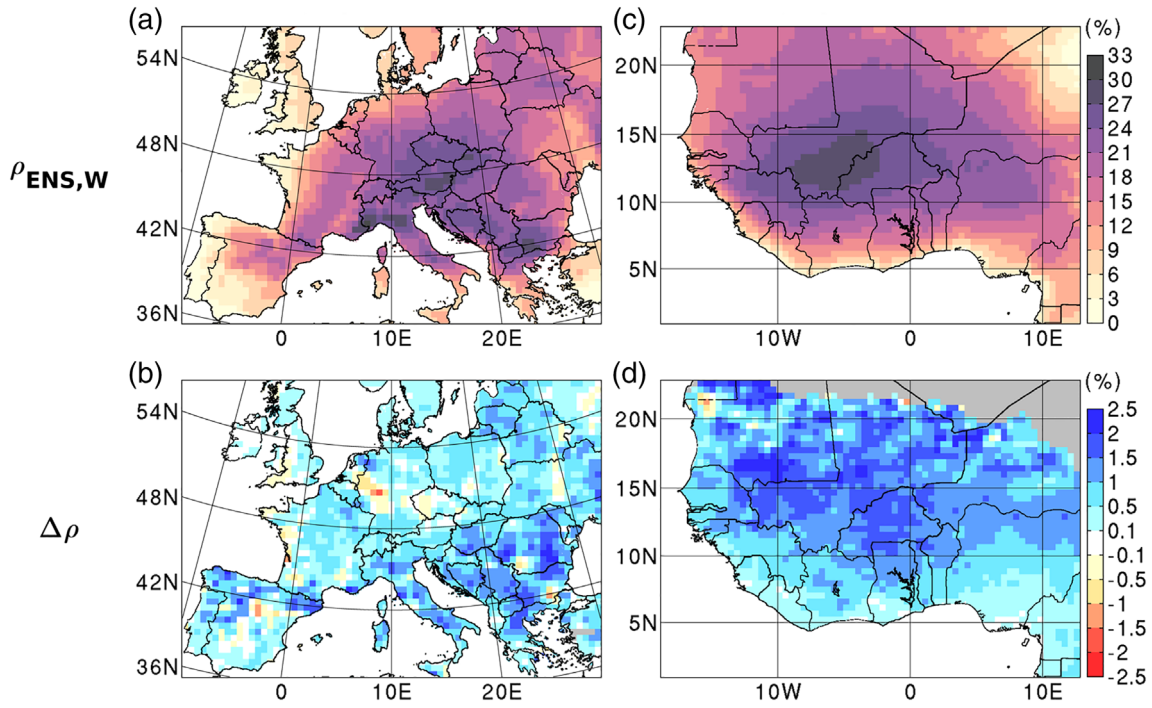

FIGURE 10 (a,b) Maps of (a) WRF-tag sub-ensemble mean of land precipitation recycling $\rho_{ENS,W}$ and (b) ensemble-mean difference in land precipitation recycling $\Delta\rho$, both temporally averaged from June to September 2008 for Europe and given in %. (c,d) As in (a,b), except for West Africa

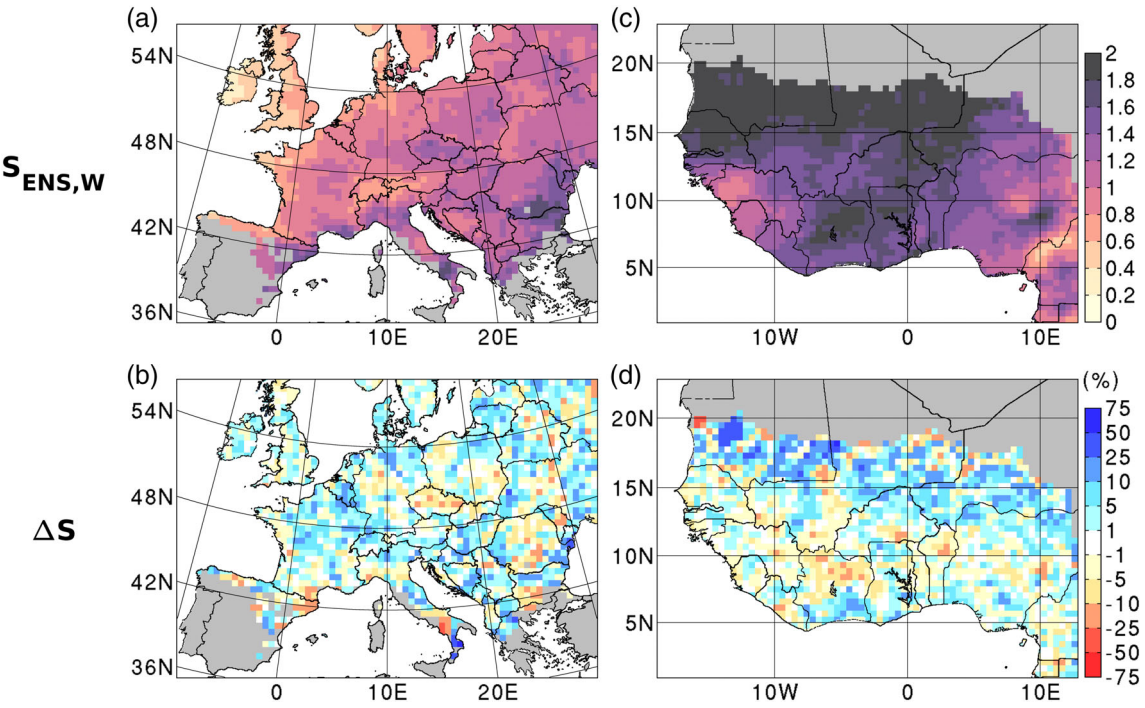

FIGURE 11 (a,b) Maps of (a) the normalized WRF-tag sub-ensemble spread of daily precipitation $S_{ENS,W}$ (−) and (b) normalized spread difference ΔS given in %, both temporally averaged from June to September 2008 for Europe. (c,d) As in (a, b), except for West Africa. The areas where an ensemble mean of daily precipitation amount above 1 mm/day occurs for less than 20 days out of the 4-month period are shaded in grey. This grey-shading is also applied to Figures 12 and 13

atmosphere coupling, and that this enhancement is slightly more pronounced in West Africa.

3.8 | Modelled precipitation uncertainty

The impact of lateral terrestrial water flow on modelled precipitation uncertainty is evaluated with the normalized ensemble spread $S_{ENS,W}$ and normalized difference ΔS in Figure 11. In order to increase the statistical significance of the displayed values of ΔS, only the areas which receive an ensemble-mean daily precipitation amount above 1 mm/day for at least 20 days out of the 4-month study period are considered in Figure 11.

The normalized ensemble spread is generally much larger in West Africa than in Europe, which means that the weather regime in West Africa is less constrained by the large-scale atmospheric condition in comparison to the weather regime in Europe. Nevertheless, the normalized ensemble spread is reduced in the mountainous areas of both regions, which shows that the strong orographic forcing on precipitation discussed by Arnault et al. (2018) in the case of Central Europe is also taking place in a tropical region.

ΔS in Figure 11 displays positive and negative areas for both Europe and West Africa, which means that lateral terrestrial water flow does not systematically enhance the modelled precipitation uncertainty. Still, the spatially averaged value of $S_{ENS,WH}$ exceeds the spatially averaged value of $S_{ENS,W}$ by 1.3% for Europe, and by 1.9% for West Africa.

In order to evaluate the model uncertainty associated with this result, the spatially-averaged difference in normalized ensemble spread is computed for all sub-ensemble combinations of size 27 within the full ensemble of size 30. It is found that this spatially-averaged difference in normalized ensemble spread varies between 0.4% and 2.5% for Europe, and between 1.4% and 2.4% for West Africa, which confirms the impact of lateral terrestrial water flow on modelled precipitation uncertainty at continental-scale.

3.9 | Land – Atmosphere coupling strength

The dependency of the impact of lateral terrestrial water flow on modelled precipitation uncertainty to the strength of the land – atmosphere coupling is assessed with the hydro-specific land precipitation recycling difference $\Delta\rho^{hydro}$ in Figure 12. For Europe, $\Delta\rho^{hydro}$ displays much more positive areas than negative areas, with a spatially averaged value of 5%. This is a clear signal that, in Europe, lateral terrestrial water flow mostly increases the modelled precipitation uncertainty when the coupling between the land and the atmosphere is enhanced, in agreement with Arnault et al. (2018)'s findings for Central Europe.

For West Africa, $\Delta\rho^{hydro}$ displays much smaller values in comparison to the case in Europe, with rather randomly distributed positive

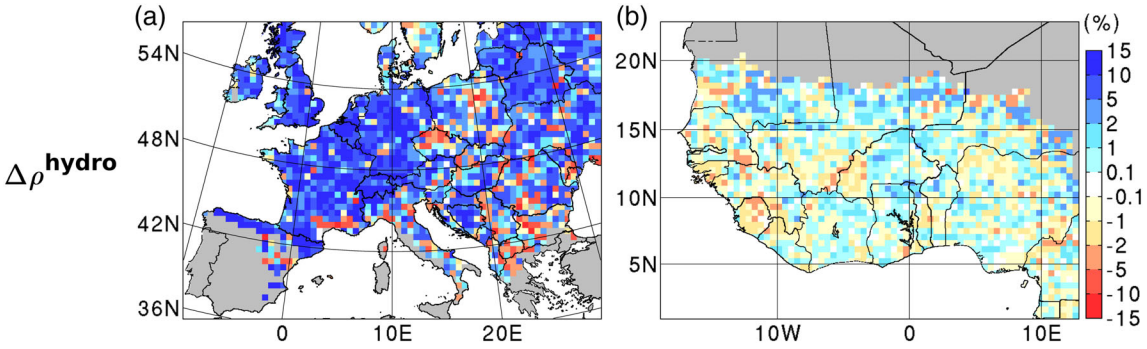

FIGURE 12 Maps of the hydro-specific land precipitation recycling difference $\Delta\rho^{hydro}$ temporally averaged from June to September 2008 for (a) Europe and (b) West Africa, given in %

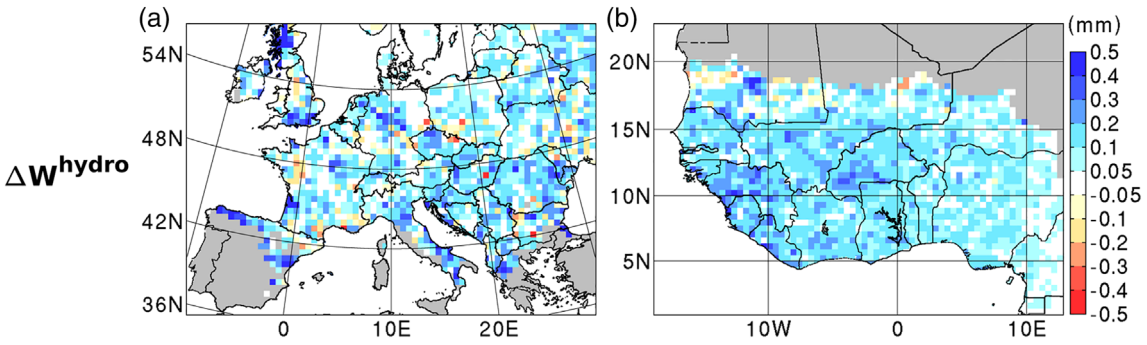

FIGURE 13 Maps of the hydro-specific atmospheric water content difference ΔW^{hydro} temporally averaged from June to September 2008 for (a) Europe and (b) West Africa, given in mm

and negative areas and a spatially averaged value below 0.1%. This is an indication that the impact of lateral terrestrial water flow on modelled precipitation uncertainty does not depend much on the strength of the land – atmosphere coupling in West Africa. An implication of this result is that no weather situation in West Africa particularly modulates the strength of the land – atmosphere coupling in such a way that it would prohibit an enhanced impact of lateral terrestrial water flow on modelled precipitation uncertainty. This is an opposite situation to that in Europe, where this impact is much reduced during weather situations characterized by a strong synoptic forcing and a weak influence of local processes (Arnault et al., 2018).

3.10 | Atmospheric wetting intensity

The dependency of the impact of lateral terrestrial water flow on modelled precipitation uncertainty to the atmospheric wetting intensity is assessed with the hydro-specific atmospheric water content difference ΔW^{hydro} in Figure 13. ΔW^{hydro} displays mostly positive values in Europe and West Africa. This means that a noticeable increase in modelled precipitation uncertainty induced by lateral terrestrial water flow is mostly associated with a comparatively larger increase in atmospheric water content induced by lateral terrestrial water flow, in both regions. Since it is known that enhanced environmental humidity favours moist convective instabilities (e.g., Derbyshire et al., 2004), we argue that the enhanced modelled precipitation uncertainty induced by lateral terrestrial water flow is a direct consequence of the atmospheric wetting effect of lateral terrestrial water flow.

4 | SUMMARY AND PERSPECTIVES

This study provides the first model evaluation of the contribution of lateral terrestrial water flow to precipitation at continental scale for Europe and West Africa. Two land surface – atmospheric models have been considered for this study, WRF-Hydro-tag which includes overland and subsurface flow, and WRF-tag which neglects lateral terrestrial water flow. WRF-tag and WRF-Hydro-tag have been set up in order to tag and trace the evaporated water from the land surface and quantify atmospheric water pathways. The evaluation of the contribution of lateral terrestrial water flow to precipitation has been achieved by comparing sub-ensembles of 30 WRF-tag simulations and 30 WRF-Hydro-tag simulations for the period June–September 2008.

For Both Europe and West Africa, lateral terrestrial water flow mostly increased land surface evaporation and precipitation through a summer-mean positive soil – moisture precipitation feedback at continental scale. In terms of ensemble mean, it was found that the relative

increase in total precipitation was of the order of 1 (±0.2)% in both continental regions, in association with a relative increase in mean land precipitation recycling by 3.6 (±0.2)% in Europe and 5. 6 (±0.2)% in West Africa. These uncertainty ranges were deduced from all combinations of subsets of 27 members out of 30. In West Africa, the relative increase in land precipitation recycling locally reached 10% north of 12°N, which suggests an enhanced sensitivity of monsoonal squall lines to lateral terrestrial water flow.

In the case of Europe, the fact that the increase in total precipitation was about two times higher than the increase in land precipitation recycling was related to an indirect pathway linking remote water sources to a change in precipitation. Indeed, the increase in land surface evaporation wetted the atmosphere, which in average increased the ability of the precipitating systems in collecting more water from remote sources and generating more precipitation. This effect could also be seen in West Africa north of 12°N. An opposite effect occurred south of 12°N, where an enhancement of the land surface evaporation contribution to precipitation was associated with a decrease of the remote water contribution to precipitation. However, the size of the ensemble was deemed to be insufficient in order to ensure that this regional dependency of the indirect pathway was not the product of modelled atmospheric randomness. Future studies addressing the spatial distribution of the indirect pathway should consider a larger ensemble size.

In both regions, lateral terrestrial water flow increased modelled precipitation uncertainty when the accumulation in atmospheric water content induced by enhanced land surface evaporation was largest, with an average increase in normalized ensemble spread of daily precipitation by 1.3% for Europe, and by 1.9% for West Africa. For Europe, the impact of lateral terrestrial water flow on modelled precipitation uncertainty was additionally modulated by the strength of the land – atmosphere coupling.

As perspective, the methodology developed in this study could be adapted in order to analyse the sensitivity of the modelled land – atmosphere system to other land processes. Ideas for future studies could be to (1) further investigate the contribution of lateral terrestrial water flow to summer precipitation with the consideration of irrigation, deep groundwater and phreatophytic plants (e.g., Boucher et al., 2004; Steward & Ahring, 2009), (2) extend the analysis of soil moisture – precipitation feedback mechanisms in Europe and West Africa for particularly dry and wet years (e.g., Gbode et al., 2019), (3) further assess the impact of vegetation dynamics on the atmospheric branch of the hydrologic cycle (e.g., Klein et al., 2017), and (4) quantify the change in simulated land – atmospheric water pathways induced by the action of constraining modelled land processes with calibrated parameters (e.g., Fersch et al., 2020). Finally, in the context of climate change mitigation, a detailed understanding of the water pathways linking a modified landuse to a precipitation change would be relevant.

ACKNOWLEDGEMENT

This research is funded by the German Science Foundation (DFG, grant AR 1183/2-1). Special thanks go to Christoph Sörgel, Ingeborg Bischoff-Gauss, Peter Weisbrod and Hartmut Häfner for the computer support.

DATA AVAILABILITY STATEMENT

The ERA5 dataset was generated using Copernicus Climate Change Service Information [2019]. Model developments and simulations with WRF-tag and WRF-Hydro-tag were performed on the computational resource ForHLR II funded by the Ministry of Science, Research and the Arts Baden-Württemberg and DFG. We acknowledge the precipitation dataset from the ECA&D project (http://www.ecad.eu) and from the Climate Hazard Center (https://www.chc.ucsb.edu/data/chirps/), and the FLUXNET surface evaporation dataset from the Max Planck Institute for Biogeochemistry (https://climatedataguide.ucar.edu/climate-data/fluxnet-mte-multi-tree-ensemble). HydroSHEDS data is available online at: https://www.hydrosheds.org/downloads, and the WRF-Hydro preprocessing tool at: https://ral.ucar.edu/projects/wrf_hydro/pre-processing-tools.

ORCID

Joël Arnault https://orcid.org/0000-0001-8859-5173
Benjamin Fersch https://orcid.org/0000-0002-4660-1165
Thomas Rummler https://orcid.org/0000-0001-7765-2275
Zhenyu Zhang https://orcid.org/0000-0002-9155-7378
Gandome Mayeul Quenum https://orcid.org/0000-0002-3666-1340
Jianhui Wei https://orcid.org/0000-0001-8609-9600
Maximilian Graf https://orcid.org/0000-0003-2246-1273
Patrick Laux https://orcid.org/0000-0002-8657-6152
Harald Kunstmann https://orcid.org/0000-0001-9573-1743

REFERENCES

Anyah, R. O., Weaver, C. P., Miguez-Macho, G., Fan, Y., & Robock, A. (2008). Incorporating water table dynamics in climate modeling: 3. Simulated groundwater influence on coupled land–atmosphere variability. *Journal of Geophysical Research*, *113*, D0703. https://doi.org/10.1029/2007JD009087

Arnault, J., Knoche, R., Wei, J., & Kunstmann, H. (2016). Evaporation tagging and atmospheric water budget analysis with WRF: A regional precipitation recycling study for West Africa. *Water Resources Research*, *52*, 1544–1567. https://doi.org/10.1002/2015WR017704

Arnault, J., Rummler, T., Baur, F., Lerch, S., Wagner, S., Fersch, B., Zhang, Z., Kerandi, N., Keil, C., & Kunstmann, H. (2018). Precipitation sensitivity to the uncertainty of terrestrial water flow in WRF-Hydro: An ensemble analysis for Central Europe. *Journal of Hydrometeorology*, *19*, 1007–1025. https://doi.org/10.1175/JHM-D-17-0042.1

Arnault, J., Wagner, S., Rummler, T., Fersch, B., Bliefernicht, J., Andresen, S., & Kunstmann, H. (2016). Role of runoff–infiltration partitioning and resolved overland flow on land–atmosphere feedbacks: A case study with the WRF-Hydro coupled modeling system for West Africa. *Journal of Hydrometeorology*, *17*, 1489–1516. https://doi.org/10.1175/JHM-D-15-0089.1

Arnault, J., Wei, J., Rummler, T., Fersch, B., Zhang, Z., Jung, G., Wagner, S., & Kunstmann, H. (2019). A joint soil-vegetation-atmospheric water tagging procedure with WRF-Hydro: Implementation and application to the case of precipitation partitioning in the upper Danube river basin. *Water Resources Research*, *55*, 6217–6243. https://doi.org/10.1029/2019WR024780

Berg, A., Findell, K., Lintner, B., Giannini, A., Seneviratne, S. I., van den Hurk, B., Lorenz, R., Pitman, A., Hagemann, S., Meier, A., Cheruy, F., Ducharne, A., Malyshev, S., & Milly, P. C. D. (2016). Land–atmosphere feedbacks amplify aridity increase over land under global warming. *Nature Climate Change*, *6*, 869–874. https://doi.org/10.1038/nclimate3029

Berg, A., Lintner, B., Findell, K., & Giannini, A. (2017). Soil moisture influence on seasonality and large-scale circulation in simulations of the West African monsoon. *Journal of Climate*, *30*, 2295–2317. https://doi.org/10.1175/JCLI-D-15-0877.1

Berner, J., Shutts, G. J., Leutbecher, M., & Palmer, T. N. (2009). A spectral stochastic kinetic energy backscatter scheme and its impact on flow-dependent predictability in the ECMWF ensemble prediction system. *Journal of the Atmospheric Sciences*, *66*, 603–626. https://doi.org/10.1175/2008JAS2677.1

Boucher, O., Myhre, G., & Myhre, A. (2004). Direct human influence of irrigation on atmospheric water vapour and climate. *Climate Dynamics*, *22*, 597–603. https://doi.org/10.1007/s00382-004-0402-4

Brubaker, K. L., Entekhabi, D., & Eagleson, P. S. (1993). Estimation of continental precipitation recycling. *Journal of Climate*, *6*, 1077–1089. https://doi.org/10.1175/1520-0442(1993)006<1077:EOCPR>2.0.CO;2

Camera, C., Bruggeman, A., Zittis, G., Sofokleous, I., & Arnault, J. (2020). Simulation of extreme rainfall and streamflow events in small Mediterranean watersheds with a one-way coupled atmospheric-hydrologic modelling system. *Natural Hazards and Earth System Sciences Discussions*, *20*, 2791–2810. https://doi.org/10.5194/nhess-2020-43

Chen, F., & Dudhia, J. (2001). Coupling an advanced land surface–hydrology model with the Penn State–NCAR MM5 modeling system. Part I: Model implementation and sensitivity. *Monthly Weather Review*, *129*, 569–585. https://doi.org/10.1175/1520-0493(2001)129<0569:CAALSH>2.0.CO;2

Copernicus Climate Change Service (C3S). (2017). *ERA5: Fifth generation of ECMWF atmospheric reanalyses of the global climate*. Copernicus Climate Change Service Climate Data Store (CDS). Retrieved from https://cds.climate.copernicus.eu/cdsapp#!/home

Cuntz, M., Mai, J., Samaniego, L., Clark, M., Wulfmeyer, V., Branch, O., Attinger, S., & Thober, S. (2016). The impact of standard and hard-coded parameters on the hydrologic fluxes in the Noah-MP land surface model. *Journal of Geophysical Research: Atmospheres*, *121*, 10676–10700. https://doi.org/10.1002/2016JD025097

Davison, J. H., Hwang, H.-T., Sudicky, E. A., Mallia, D. V., & Lin, J. C. (2018). Full coupling between the atmosphere, surface, and subsurface for integrated hydrologic simulation. *Journal of Advances in Modeling Earth Systems*, *10*, 43–53. https://doi.org/10.1002/2017MS001052

Derbyshire, S. H., Beau, I., Bechtold, P., Grandpeix, J.-Y., Piriou, J.-M., Redelsperger, J.-L., & Soares, P. M. M. (2004). Sensitivity of moist convection to environmental humidity. *Quarterly Journal of the Royal Meteorological Society*, *130*, 3055–3079. https://doi.org/10.1256/qj.03.130

Dirmeyer, P. A., Cash, B. A., Kinter, J. L., Stan, C., Jung, T., Marx, L., Towers, P., Wedi, N., Adams, J., Altshuler, E., Huang, B., Jin, E., & Manganello, J. (2012). Evidence for enhanced land–atmosphere feedback in a warming climate. *Journal of Hydrometeorology*, *13*, 981–995. https://doi.org/10.1175/JHM-D-110104.1

Dirmeyer, P. A., Jin, Y., Singh, B., & Yan, X. (2013). Trends in land–atmosphere interactions from CMIP5 simulations. *Journal of Hydrometeorology*, *14*, 829–849. https://doi.org/10.1175/JHM-D-12-0107.1

Dirmeyer, P. A., Schlosser, C. A., & Brubaker, K. L. (2009). Precipitation, recycling, and land memory: An integrated analysis. *Journal of Hydrometeorology*, *10*, 278–288. https://doi.org/10.1175/2008JHM1016.1

Dominguez, F., Miguez-Macho, G., & Hu, H. (2016). WRF with water vapor tracers: A study of moisture sources for the North American Monsoon. *Journal of Hydrometeorology*, *17*, 1915–1927. https://doi.org/10.1175/JHM-D-15-0221.1

Dudhia, J. (1989). Numerical study of convection observed during the Winter Monsoon Experiment using a mesoscale two-dimensional model. *Journal of the Atmospheric Sciences*, *46*, 3077–3107. https://doi.org/10.1175/1520-0469(1989)046<3077:NSOCOD>2.0.CO;2

Errico, R. M., Langland, R., & Baumhefner, D. P. (2002). The workshop in atmospheric predictability. *Bulletin of the American Meteorological Society*, *83*, 1341–1344.

FAO. (1991). *The digitized soil map of the world* (World Soil Resource Rep. 67), FAO, Rome, Italy.

Fersch, B., Senatore, A., Adler, B., Arnault, J., Mauder, M., Schneider, K., Völksch, I., & Kunstmann, H. (2020). High-resolution fully-coupled atmospheric–hydrological modeling: A cross-compartment regional water and energy cycle evaluation. *Hydrology and Earth System Sciences*, *24*, 2457–2481. https://doi.org/10.5194/hess-24-2457-2020

Friedl, M. A., Mc Iver, D. K., Hodges, J. C. F., Zhang, X. Y., Muchoney, D., Strahler, A. H., Gopal, C. E. W. S., Schneider, A., Cooper, A., Baccini, A., Gao, F., & Schaaf, C. (2002). Global land cover mapping from MODIS: Algorithms and early results. *Remote Sensing of Environment*, *83*, 287–302. https://doi.org/10.1016/S0034-4257(02)00078-0

Funk, C., Peterson, P., Landsfeld, M., Pedreros, D., Verdin, J., Shukla, S., Husak, G., Rowland, J., Harrison, L., Hoell, A., & Michaelsen, J. (2015). The climate hazards infrared precipitation with stations—A new environmental record for monitoring extremes. *Scientific Data*, *2*, 150066. https://doi.org/10.1038/sdata.2015.66

Gbode, I. E., Ogunjobi, K. O., Dudhia, J., & Ajayi, V. O. (2019). Simulation of wet and dry West African monsoon rainfall seasons using the Weather Research and Forecasting model. *Theoretical and Applied Climatology*, *138*, 1679–1694. https://doi.org/10.1007/s00704-019-02912-x

Gerken, T., Ruddell, B. L., Yu, R., Stoy, P. C., & Drewry, D. T. (2019). Robust observations of land-to-atmosphere feedbacks using the information flows of FLUXNET. *npj Climate and Atmospheric Science*, *2*, 37. https://doi.org/10.1038/s41612-019-0094-4

Gochis, D. J., Barlage, M., Dugger, A., FitzGerald, K., Karsten, L., McAllister, M., McCreight, J., Mills, J., RafieeiNasab, A., Read, L., Sampson, K., Yates, D., & Yu, W. (2018). *The WRF-Hydro modeling system technical description, (Version 5.0)*. NCAR Technical Note, p. 107. Retrieved from https://ral.ucar.edu/projects/wrf_hydro/technical-description-user-guide. Source Code doi:https://doi.org/10.5065/D6J38RBJ

Haylock, M. R., Hofstra, N., Klein Tank, A. M. G., Klok, E. J., Jones, P. D., & New, M. (2008). A European daily high-resolution gridded dataset of surface temperature and precipitation. *Journal of Geophysical Research: Atmospheres*, *113*, D20119. https://doi.org/10.1029/2008JD010201

Hohenegger, C., Walser, A., Langhans, W., & Schär, C. (2008). Cloud-resolving ensemble simulations of the August 2005 Alpine flood. *Quarterly Journal of the Royal Meteorological Society*, *134*, 889–904. https://doi.org/10.1002/qj.252

Hong, S.-Y., & Lim, J.-O. J. (2006). The WRF single-moment 6-class microphysics scheme (WSM6). *Journal of the Korean Meteorological Society*, *42*, 129–151.

Hsu, H., Lo, M.-H., Guillod, B. P., Miralles, D. G., & Kumar, S. (2017). Relation between precipitation location and antecedent/subsequent soil moisture spatial patterns. *Journal of Geophysical Research: Atmosphere*, *122*, 6319–6328. https://doi.org/10.1002/2016JD026042

Insua-Costa, D., & Miguez-Macho, G. (2018). A new moisture tagging capability in the Weather Research and Forecasting model: Formulation, validation and application to the 2014 Great Lake-effect snowstorm. *Earth System Dynamics*, *9*, 167–185. https://doi.org/10.5194/esd-9-167-2018

Jung, M., Reichstein, M., & Bondeau, A. (2009). Towards global empirical upscaling of FLUXNET eddy covariance observations: Validation of a model tree ensemble approach using a biosphere model. *Biogeosciences*, *6*, 2001–2013. https://doi.org/10.5194/bg-6-2001-2009

Jung, M., Reichstein, M., Ciais, P., Seneviratne, S. I., Sheeld, J., Goulden, M. L., Bonan, G., Cescatti, A., Chen, J., de Jeu, R., Dolman, A. J., Eugster, W., Gerten, D., Gianelle, D., Gobron, N., Heinke, J., Kimball, J., Law, B. E., Montagnani, L., … Zhang, K. (2010). Recent decline in the global land evapotranspiration trend due to limited moisture supply. *Nature*, *467*, 951–954. https://doi.org/10.1038/nature09396

Keil, C., Heinlein, F., & Craig, G. C. (2014). The convective adjustment time-scale as indicator of predictability of convective precipitation. *Quarterly Journal of the Royal Meteorological Society*, *140*, 480–490. https://doi.org/10.1002/qj.2143

Klein, C., Bliefernicht, J., Heinzeller, D., Gessner, U., Klein, I., & Kunstmann, H. (2017). Feedback of observed interannual vegetation change: A regional climate model analysis for the West African monsoon. *Climate Dynamics*, *48*, 2837–2858. https://doi.org/10.1007/s00382-016-3237-x

Knist, S., Goergen, K., Buonomo, E., Christensen, O. B., Colette, A., Cardoso, R. M., Fealy, R., Fernández, J., García-Díez, M., Jacob, D., Kartsios, S., Katragkou, E., Keuler, K., Mayer, S., van Meijgaard, E., Nikulin, G., Soares, P. M. M., Sobolowski, S., Szepszo, G., … Simmer, C. (2017). Land-atmosphere coupling in EURO-CORDEX evaluation experiments. *Journal of Geophysical Research: Atmospheres*, *122*, 79–103. https://doi.org/10.1002/2016JD025476

Knoche, H. R., & Kunstmann, H. (2013). Tracking atmospheric water pathways by direct evaporation tagging: A case study for West Africa. *Journal of Geophysical Research: Atmospheres*, *118*, 12345–12358. https://doi.org/10.1002/2013JD019976

Koster, R. D., Chang, Y., Wang, H., & Schubert, S. D. (2016). Impacts of local soil Moisture anomalies on the atmospheric circulation and on remote surface meteorological fields during boreal summer: A comprehensive analysis over north America. *Journal of Climate*, *29*, 7345–7364. https://doi.org/10.1175/JCLI-D-160192.1

Kumar, A., Chen, F., Barlage, M., Ek, M. B., & Niyogi, D. (2014). Assessing impacts of integrating MODIS vegetation data in the weather research and forecasting (WRF) model coupled to two different canopy-resistance approaches. *Journal of Applied Meteorology and Climatology*, *53*, 1362–1380. https://doi.org/10.1175/JAMC-D-13-0247.1

Laing, A. G., Carbone, R. E., Levizzani, V., & Tuttle, J. D. (2008). The propagation and diurnal cycles of deep convection in northern tropical Africa. *Quarterly Journal of the Royal Meteorological Society*, *134*, 93–109. https://doi.org/10.1002/qj.194

Larsen, M. A. D., Christensen, J. H., Drews, M., Butts, M. B., & Refsgaard, J. C. (2016). Local control on precipitation in a fully coupled climate-hydrology model. *Scientific Reports*, *6*, 22927. https://doi.org/10.1038/srep22927

Laux, P., Nguyen, P. N. B., Cullmann, J., Van, T. P., & Kunstmann, H. (2017). How many RCM ensemble members provide confidence in the impact of land-use land cover change? *International Journal of Climatology*, *37*, 2080–2100. https://doi.org/10.1002/joc.4836

Lehner, B., Verdin, K., & Jarvis, A. (2008). New global hydrography derived from spaceborne elevation data. *Eos, Transactions, American Geophysical Union*, *89*(10), 93–94. https://doi.org/10.1029/2008EO100001

Li, L., Pontoppidan, M., Sobolowski, S., & Senatore, A. (2020). The impact of initial conditions on convection-permitting simulations of a flood event over complex mountainous terrain. *Hydrology and Earth System Sciences*, *24*, 771–791. https://doi.org/10.5194/hess-24-771-2020

Lorenz, E. N. (1969). The predictability of a flow which possesses many scales of motion. *Tellus*, *21*, 289–307. https://doi.org/10.1111/j.2153-3490.1969.tb00444.x

Marsham, J. H., Dixon, N. S., Garcia-Carreras, L., Lister, G. M. S., Parker, D. J., Knippertz, P., & Birch, C. E. (2013). The role of moist convection in the West African monsoon system: Insights from continental-scale convection-permitting simulations. *Geophysical Research Letters*, *40*, 1843–1849. https://doi.org/10.1002/grl.50347

Maxwell, R. M., Lundquist, J. K., Mirocha, J. D., Smith, S. G., Woodward, C. S., & Tompson, A. F. (2011). Development of a coupled groundwater-atmosphere model. *Monthly Weather Review*, *139*, 96–116. https://doi.org/10.1175/2010MWR3392.1

Mlawer, E. J., Taubman, S. J., Brown, P. D., Iacono, M. J., & Clough, S. A. (1997). Radiative transfer for inhomogeneous atmosphere: RRTM, a validated correlated-k model for the long-wave. *Journal of Geophysical Research*, *102*(D14), 16663–16682. https://doi.org/10.1029/97JD00237

Niu, G.-Y., Yang, Z.-L., Mitchell, K. E., Chen, F., Ek, M. B., Barlage, M., Kumar, A., Manning, K., Niyogi, D., Rosero, E., Tewari, M., & Xia, Y. (2011). The community Noah land surface model with multiparameterization options (Noah-MP): 1. Model description and evaluation with local-scale measurements. *Journal of Geophysical Research*, *116*, D12109. https://doi.org/10.1029/2010JD015139

Peters, K., Jakob, C., Davies, L., Khouider, B., & Majda, A. J. (2013). Stochastic behavior of tropical convection in observations and a multicloud model. *Journal of the Atmospheric Sciences*, *70*, 3556–3575. https://doi.org/10.1175/JAS-D-13-031.1

Pleim, J. E. (2007). A combined local and nonlocal closure model for the atmospheric boundary layer. Part I: Model description and testing. *Journal of Applied Meteorology and Climatology*, *46*, 1383–1395. https://doi.org/10.1175/JAM2539.1

Prein, A. F., Gobiet, A., Truhetz, H., Keuler, K., Goergen, K., Teichmann, C., Fox Maule, C., van Meijgaard, E., Déqué, M., Nikulin, G., Vautard, R., Colette, A., Kjellström, E., & Jacob, D. (2016). Precipitation in the EURO-CORDEX 0.11° and 0.44° simulations: High resolution, high benefits? *Climate Dynamics*, *46*, 383–412. https://doi.org/10.1007/s00382-015-2589-y

Rahman, M., Sulis, M., & Kollet, S. J. (2015). The subsurface–land surface–atmosphere connection under convective conditions. *Advances in Water Resources*, *83*, 240–249. https://doi.org/10.1016/j.advwatres.2015.06.003

Rasmussen, S. H., Christensen, J. H., Drews, M., Gochis, D. J., & Refsgaard, J. C. (2012). Spatial-scale characteristics of precipitation simulated by regional climate models and the implications for hydrological modeling. *Journal of Hydrometeorology*, *13*, 1817–1835. https://doi.org/10.1175/JHM-D-12-07.1

Rummler, T., Arnault, J., Gochis, D., & Kunstmann, H. (2019). Role of lateral terrestrial water flow on the regional water cycle in a complex terrain region: Investigation with a fully coupled model system. *Journal of Geophysical Research: Atmospheres*, *124*, 507–529. https://doi.org/10.1029/2018JD029004

Schaake, J. C., Koren, V. I., Duan, Q.-Y., Mitchell, K., & Chen, F. (1996). Simple water balance model for estimating runoff at different spatial and temporal scales. *Journal of Geophysical Research*, *101*, 7461–7475. https://doi.org/10.1029/95JD02892

Senatore, A., Furnari, L., & Mendicino, G. (2020). Impact of high-resolution sea surface temperature representation on the forecast of small Mediterranean catchments' hydrological responses to heavy precipitation. *Hydrology and Earth System Sciences*, *24*, 269–291. https://doi.org/10.5194/hess-24-269-2020

Seneviratne, S. I., Corti, T., Davin, E. L., Hirschi, M., Jaeger, E. B., Lehner, I., Orlowsky, B., & Teuling, A. J. (2010). Investigating soil moisture–climate interactions in a changing climate: A review. *Earth-Science Reviews*, *99*(3-4), 125–161. https://doi.org/10.1016/j.earscirev.2010.02.004

Shutts, G. J. (2005). A kinetic energy backscatter algorithm for use in ensemble prediction systems. *Quarterly Journal of the Royal Meteorological Society*, *131*, 3079–3102. https://doi.org/10.1256/qj.04.106

Skamarock, W. C., & Klemp, J. B. (2008). A time-split nonhydrostatic atmospheric model for weather research and forecasting applications. *Journal of Computational Physics*, *227*, 3465–3485. https://doi.org/10.1016/j.jcp.2007.01.037

Sodemann, H., Wernli, H., & Schwierz, C. (2009). Sources of water vapour contributing to the Elbe flood in August 2002—A tagging study in a mesoscale model. *Quarterly Journal of the Royal Meteorological Society*, *135*, 205–223. https://doi.org/10.1002/qj.374

Sprenger, M., Seeger, S., Blume, T., & Weiler, M. (2016). Travel times in the vadose zone: Variability in space and time. *Water Resources Research*, *52*, 5727–5754. https://doi.org/10.1002/2015WR018077

Steward, D. R., & Ahring, T. S. (2009). An analytic solution for groundwater uptake by phreatophytes spanning spatial scales from plant to field to regional. *Journal of Engineering Mathematics*, *64*, 85–103. https://doi.org/10.1007/s10665-008-9255-x

Sulis, M., Keune, J., Shrestha, P., Simmer, C., & Kollet, S. J. (2018). Quantifying the impact of subsurface-land surface physical processes on the predictive skill of subseasonal mesoscale atmospheric simulations. *Journal of Geophysical Research: Atmospheres*, *123*, 9131–9151. https://doi.org/10.1029/2017JD028187

Taylor, C. M., de Jeu, R. A. M., Guichard, F., Harris, P. P., & Dorigo, W. A. (2012). Afternoon rain more likely over drier soils. *Nature*, *489*, 423–426. https://doi.org/10.1038/nature11377

Teng, H., Branstator, G., Tawfik, A. B., & Callaghan, P. (2019). Circumglobal response to prescribed soil moisture over north America. *Journal of Climate*, *32*, 4525–4545. https://doi.org/10.1175/JCLI-D-18-0823.1

Trenberth, K. E. (1999). Atmospheric moisture recycling: Role of advection and local evaporation. *Journal of Climate*, *12*, 1368–1381. https://doi.org/10.1175/1520-0442(1999)012<1368:AMRROA>2.0.CO;2

van der Ent, R.,. J., Savenije, H. H. G., Schaefli, B., & Steele-Dunne, S. C. (2010). Origin and fate of atmospheric moisture over continents. *Water Resources Research*, *46*, W09525. https://doi.org/10.1029/2010WR009127

Wagner, S., Fersch, B., Yuan, F., Yu, Z., & Kunstmann, H. (2016). Fully coupled atmospheric-hydrological modeling at regional and long-term scales: Development, application, and analysis of WRF-HMS. *Water Resources Research*, *52*, 3187–3211. https://doi.org/10.1002/2015WR018185

Wei, J., & Dirmeyer, P. A. (2019). Sensitivity of land precipitation to surface evapotranspiration: A nonlocal perspective based on water vapor transport. *Geophysical Research Letters*, *46*, 12588–12597. https://doi.org/10.1029/2019GL085613

Wei, J., Knoche, H. R., & Kunstmann, H. (2015). Contribution of transpiration and evaporation to precipitation: An ET-Tagging study for the Poyang Lake region in Southeast China. *Journal of Geophysical Research: Atmospheres*, *120*, 6845–6864. https://doi.org/10.1002/2014JD022975

Wei, J., Knoche, H. R., & Kunstmann, H. (2016). Atmospheric residence times from transpiration and evaporation to precipitation: An age-weighted regional evaporation tagging approach. *Journal of Geophysical Research: Atmospheres*, *121*, 6841–6862. https://doi.org/10.1002/2015JD024650

Xue, Y., Boone, A., & Taylor, C. M. (2012). Review of recent developments and the future prospective in West African atmosphere/land interaction studies. *International Journal of Geophysics*, *2012*, 1–12. https://doi.org/10.1155/2012/748921

Zhang, Z., Arnault, J., Wagner, S., Laux, P., & Kunstmann, H. (2019). Impact of lateral terrestrial water flow on land-atmosphere interactions in the Heihe River Basin in China: Fully coupled modeling and precipitation recycling analysis. *Journal of Geophysical Research: Atmospheres*, *124*, 8401–8423. https://doi.org/10.1029/2018JD030174

Zhou, S., Williams, A. P., Berg, A. M., Cook, B. I., Zhang, Y., Hagemann, S., Lorenz, R., Seneviratne, S. I., & Gentine, P. (2019). Land–atmosphere feedbacks exacerbate concurrent soil drought and atmospheric aridity. *Proceedings of the National Academy of Sciences of the United States of America*, *116*, 18848–18853. https://doi.org/10.1073/pnas.1904955116

Zveryaev, I. I., & Allan, R. P. (2010). Summertime precipitation uncertainty over Europe and its links to atmospheric dynamics and evaporation. *Journal of Geophysical Research*, *115*, D12102. https://doi.org/10.1029/2008JD011213

How to cite this article: Arnault J, Fersch B, Rummler T, et al. Lateral terrestrial water flow contribution to summer precipitation at continental scale – A comparison between Europe and West Africa with WRF-Hydro-tag ensembles. *Hydrological Processes*. 2021;35:e14183. https://doi.org/10.1002/hyp.14183